AD-A042 547 STANFORD RESEARCH INST MENLO PARK CALIF F/G 18/3
LABORATORY INVESTIGATION OF STEMMING AND CONTAINMENT IN UNDERGR--ETC(U)
OCT 76 A L FLORENCE DNA001-75-C-0083
UNCLASSIFIED DNA-4149F NL

1 OF 1
ADA042547

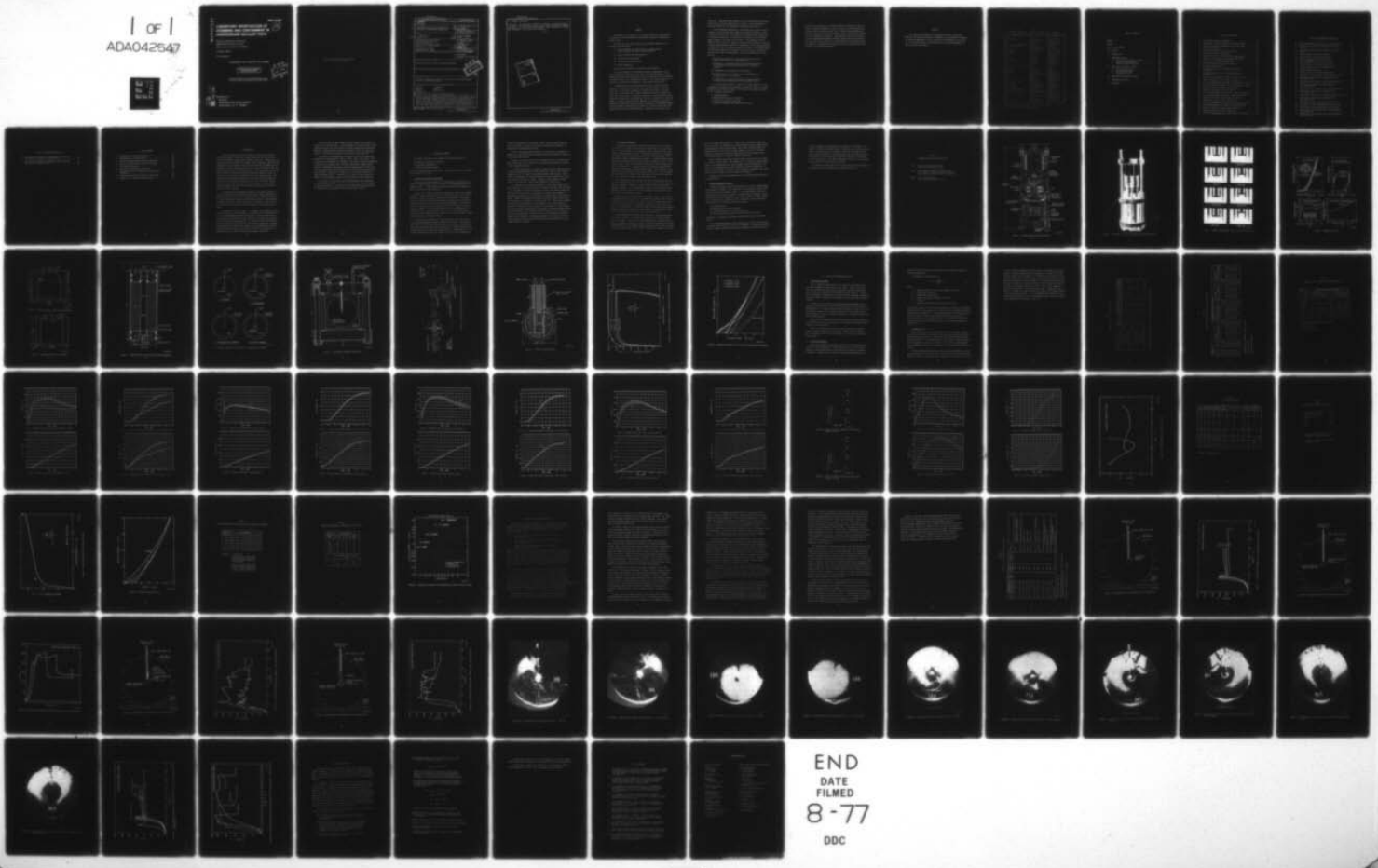

END
DATE FILMED
8-77
DDC

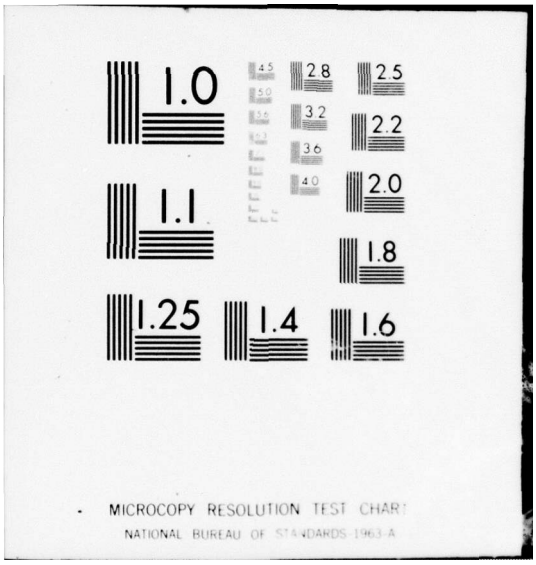
1.0
1.1
1.25
1.4
1.6
1.8
2.0
2.2
2.5
2.8
3.2
3.6
4.0
4.5
5.0
MICROCOPY RESOLUTION TEST CHART
NATIONAL BUREAU OF STANDARDS-1963-A

DNA 4149F

LABORATORY INVESTIGATION OF STEMMING AND CONTAINMENT IN UNDERGROUND NUCLEAR TESTS

Stanford Research Institute
333 Ravenswood Avenue
Menlo Park, California 94025

October 1976

Final Report

CONTRACT No. DNA 001-75-C-0083

THIS WORK SPONSORED BY THE DEFENSE NUCLEAR AGENCY
UNDER RDT&E RMSS CODE B344075462 J24AAXYS98426 H2590D.

Prepared for
Director
DEFENSE NUCLEAR AGENCY
Washington, D. C. 20305

Destroy this report when it is no longer
needed. Do not return to sender.

UNCLASSIFIED

SECURITY CLASSIFICATION OF THIS PAGE *(When Data Entered)*

19 REPORT DOCUMENTATION PAGE	READ INSTRUCTIONS BEFORE COMPLETING FORM
1. REPORT NUMBER: DNA 4149F	2. GOVT ACCESSION NO. / 3. RECIPIENT'S CATALOG NUMBER
4. TITLE *(and Subtitle)*: LABORATORY INVESTIGATION OF STEMMING AND CONTAINMENT IN UNDERGROUND NUCLEAR TESTS	5. TYPE OF REPORT & PERIOD COVERED: Final Report.
	6. PERFORMING ORG. REPORT NUMBER: SRI Project PYU-3702
7. AUTHOR(s): A. L. Florence	8. CONTRACT OR GRANT NUMBER(s): DNA 001-75-C-0083
9. PERFORMING ORGANIZATION NAME AND ADDRESS: Stanford Research Institute, 333 Ravenswood Avenue, Menlo Park, California 94025	10. PROGRAM ELEMENT, PROJECT, TASK AREA & WORK UNIT NUMBERS: DNA NWET — Subtask J24AAXYS984-26
11. CONTROLLING OFFICE NAME AND ADDRESS: Director, Defense Nuclear Agency, Washington, D.C. 20305	12. REPORT DATE: October 1976
	13. NUMBER OF PAGES: ~~90~~ 12 88p.
14. MONITORING AGENCY NAME & ADDRESS *(if different from Controlling Office)*	15. SECURITY CLASS *(of this report)*: UNCLASSIFIED
	15a. DECLASSIFICATION/DOWNGRADING SCHEDULE

16. DISTRIBUTION STATEMENT *(of this Report)*

Approved for public release; distribution unlimited.

17. DISTRIBUTION STATEMENT *(of the abstract entered in Block 20, if different from Report)*

18. SUPPLEMENTARY NOTES

This work sponsored by the Defense Nuclear Agency under RDT&E RMSS Code B344075462 J24AAXYS98426 H2590D.

19. KEY WORDS *(Continue on reverse side if necessary and identify by block number)*

Stemming	Containment
Extrusion	Cavity
Nuclear	Hydrofracture
Underground	

20. ABSTRACT *(Continue on reverse side if necessary and identify by block number)*

As part of the DNA stemming and containment program for underground nuclear testing, laboratory investigations were carried out in three areas: generation of experimental results suitable for correlation with predictions of computer codes used in DNA grout flow calculations, development of a containment experiment for studying residual stress fields around exploded cavities, and a theoretical analysis for studying the residual stress fields. Grout flow results were generated and supplied in a form suitable for code

DD FORM 1 JAN 73 1473 EDITION OF 1 NOV 65 IS OBSOLETE

UNCLASSIFIED

SECURITY CLASSIFICATION OF THIS PAGE *(When Data Entered)*

332 500

20. ABSTRACT (Continued)

correlation. The containment experiment was brought to an advanced stage of development. The theoretical analysis, based on many simplifying assumptions, was completed up to the second cavity expansion stage, resulting in a reasonable description of the stress field formation.

SUMMARY

The purpose of this project is to conduct laboratory investigations in support of the DNA stemming and containment program for underground nuclear tests.

Over the years, the DNA stemming and containment program has consisted of five main parts:

(1) Code development and application for ground motion, tunnel closure, and grout flow calculations.

(2) Material properties determination.

(3) Laboratory investigations.

(4) Scaled high explosive tests.

(5) Field diagnostics.

SRI has been conducting the laboratory investigations.

During this phase of the laboratory program, experimental results were generated for correlation with grout flow code predictions, a containment experiment was developed to study the residual stress surrounding an exploded cavity in a rheological material, and a simple analysis was performed to describe the formation of the residual stress field.

A dynamic grout extrusion technique was used to generate results suitable for correlation with grout flow code predictions. With this technique, a cylindrical specimen of superlean grout (SLG) in a heavy steel tube is extruded into a coaxial transparent tunnel of smaller diameter by a steel piston. The piston is driven by a well defined pressure pulse and the motion of the piston and SLG front is observed by high speed camera. Colored ceramic beads are embedded in the grout to observe the initial and final positions of an array of particles. An auxiliary experiment was devised and used twice to obtain the friction between SLG under pressure and the steel container walls. Properties of the grout were

determined. Recommended improvements to the technique are more precise control over the grout properties and further friction experiments to establish reliability and dependence on pressure and velocity.

In the containment experiment, a small spherical charge is cast in a sphere of rock matching grout (RMG) with properties similar to those of Nevada Test Site tuff. The RMG sphere is hydraulically pressurized to represent overburden. The explosive is detonated and the residual gases released by drilling into the cavity. Dyed glycerol fluid is pumped into the cavity at a constant flow rate until fracture occurs and a steady radial pressure gradient is established. The internal pressure is removed and then the external pressure is removed. The cracked sphere is drained and tapped into two parts by use of a chisel, and each exposed fracture plane is photographed. The main observations of this work are

- Hydrofracture pressures in an exploded cavity were 50% higher than those in an unexploded cavity.
- Existence of a residual stress field was demonstrated by the increased hydrofracture pressure and by fracture patterns.
- Permeability was decreased by the explosion.
- Reproducibility of the hydrofracture experiments with an unexploded cavity was good.
- Further work is required to demonstrate reproducibility of hydrofracture experiments with an exploded cavity.

In the containment analysis, a gas with a known equation of state is assumed to instantaneously pressurize a spherical cavity in a solid homogeneous and isotropic medium. The analysis was rendered tractable by the following idealizations:

- Incompressibility
- Elastic-perfectly plastic behavior
- Yielding by the Mises condition
- Plastic straining by the associated flow rule.

Overburden is included as a constant pressure infinitely far from the cavity. Numerical examples are used to describe cavity expansion and formation of the residual stress field. Predictions generally agree with the predictions of finite-difference codes; cavity expansion agrees with the containment experiment. Formulas were derived for estimates of cavity expansion and maximum residual stresses and their locations. The next step in the analysis is to incorporate a yield condition that is stronger in compression than tension to make the analysis more representative of rheological materials.

PREFACE

The authors are indebted to the technical monitor, Carl Keller (DNA FTD) for ideas and guidance, to members of the containment community for helpful suggestions, to Scott Butters and Dan Gardener of Terra Tek, Inc. for material property determination, and to George Abrahamson for overall project supervision.

Table

CONVERSION FACTORS FOR U.S. CUSTOMARY TO METRIC (SI) UNITS OF MEASUREMENT

To Convert From	To	Multiply By
angstrom	meters (m)	1.000 000 × E -10
atmosphere (normal)	kilo pascal (kPa)	1.013 25 × E +2
bar	kilo pascal (kPa)	1.000 000 × E +2
barn	meter^2 (m^2)	1.000 000 × E -28
British thermal unit (thermochemical)	joule (J)	1.054 350 × E +3
calorie (thermochemical)	joule (J)	4.184 000
cal (thermochemical)/cm^2	mega joule/m^2 (MJ/m^2)	4.184 000 × E -2
curie	giga becquerel (GBq)*	3.700 000 × E +1
degree (angle)	radian (rad)	1.745 329 × E -2
degree Fahrenheit	degree kelvin (K)	$t_k = (t°f + 459.67)/1.8$
electron volt	joule (J)	1.602 19 × E -19
erg	joule (J)	1.000 000 × E -7
erg/second	watt (W)	1.000 000 × E -7
foot	meter (m)	3.048 000 × E -1
foot-pound-force	joule (J)	1.355 818
gallon (U.S. liquid)	meter^3 (m^3)	3.785 412 × E -3
inch	meter (m)	2.540 000 × E -2
jerk	joule (J)	1.000 000 × E +9
joule/kilogram (J/kg) (radiation dose absorbed)	Gray (Gy)	1.000 000
kilotons	terajoules	4.183
kip (1000 lbf)	newton (N)	4.448 222 × E +3
kip/inch^2 (ksi)	kilo pascal (kPa)	6.894 757 × E +3
ktap	newton-second/m^2 ($N-s/m^2$)	1.000 000 × E +2
micron	meter (m)	1.000 000 × E -6
mil	meter (m)	2.540 000 × E -5
mile (international)	meter (m)	1.609 344 × E +3
ounce	kilogram (kg)	2.834 952 × E -2
pound-force (lbf avoirdupois)	newton (N)	4.448 222
pound-force inch	newton-meter (N-m)	1.129 848 × E -1
pound-force/inch	newton/meter (N/m)	1.751 268 × E +2
pound-force/foot^2	kilo pascal (kPa)	4.788 026 × E -2
pound-force/inch^2 (psi)	kilo pascal (kPa)	6.894 757
pound-mass (lbm avoirdupois)	kilogram (kg)	4.535 924 × E -1
pound-mass-foot^2 (moment of inertia)	kilogram-meter^2 (kg/m^2)	4.214 011 × E -2
pound-mass/foot^3	kilogram/meter^3 (kg/m^3)	1.601 846 × E +1
rad (radiation dose absorbed)	Gray (Gy)†	1.000 000 × E -2
roentgen	coulomb/kilogram (C/kg)	2.579 760 × E -4
shake	second (s)	1.000 000 × E -8
slug	kilogram (kg)	1.459 390 × E +1
torr (mm Hg, 0°C)	kilo pascal (kPa)	1.333 22 × E -1

*The becquerel (Bq) is the SI unit of radioactivity; 1 Bq = 1 event/s.

†The Gray (Gy) is the SI unit of absorbed radiation.

TABLE OF CONTENTS

LIST OF ILLUSTRATIONS

LIST OF ILLUSTRATIONS (Continued)

LIST OF ILLUSTRATIONS (Continued)

LIST OF TABLES

I INTRODUCTION

During an underground nuclear explosion, the burst of radiation that travels along a steel line-of-sight vacuum pipe to the test stations is followed by ground shock collapse of the pipe. Energy flow from the source and the violent pipe collapse form a plasma jet, which must be stopped before the plasma can reach the test stations and damage the experiments. Devices like mufflers and doors delay the plasma so that the ground shock can seal the pipe ahead of it. The tunnel space around the pipe is filled with grout to provide mechanical coupling, so that, on closure, the tunnel becomes filled with grout and broken-up pipe. The ground motion ceases more rapidly than the grout motion so that grout continues to flow along the tunnel for some time. This grout flow is also aided by the gas pressure in the device cavity. In a successful stemming scheme, this late-time extrusion is halted before the grout reached the test stations.

The spherically diverging ground motion is eventually brought to rest by outward energy radiation of stress waves, energy dissipation of crushing, distortion, and crack formation, and the combined resistance of tensile tangential stresses and overburden pressure. This combined resistance eventually causes a rebound of the medium that may cause further plastic work around the cavity and intensify the residual stress field.

In underground nuclear tests, it is required that radioactive gases not be released into the atmosphere. In general, this requirement will be met if experimental tunnels leading from the nuclear device cavity are stemmed successfully and if the residual cavity gases are contained by the adjacent surrounding medium. The residual stress field created around the cavity by the explosion probably aids containment. Although containment has been achieved for many years and stemming has generally been successful in recent nuclear tests, reliability is uncertain and planned tests still require extensive containment evaluation.

Over the years, the DNA stemming and containment (SAC) program has consisted of five main parts: code development for ground motion, tunnel closure, and grout flow calculations, material properties determination, laboratory investigations, scaled high explosive tests, and field diagnostics. SRI has been conducting the laboratory investigations.[1-4]

Our laboratory investigations during the last year are completely documented in Topical Reports 3702-1, 3702-2, 3702-3, and 3702-4. This report serves to summarize our findings. The areas of research summarized in Section II are dynamic grout extrusion experiments (Topical Report 3702-4),[5] experiments developed to study the residual stress field surrounding an exploded cavity (Topical Report 3702-3),[6] and a simple analysis performed to describe the formation of the residual stress field (Topical Report 3702-2).[7] Sections III, IV, and V of this report summarize the developmental progress and the principal results obtained.

At the start of this year's work, photoplasticity was considered for investigating residual stress fields caused by the dynamic expansion of holes and cavities. The work led to the conclusion that the method is unsuitable and is described in SRI Topical Report 3702-1.[8]

II LABORATORY PROGRAM

The three main areas of the ongoing SAC laboratory study are

- Dynamic SLG extrusion experiments
- Containment experiments
- Simple containment analysis.

These investigations are described here. The main results are presented in Sections III, IV, and V.

A. Dynamic SLG Extrusion Experiments

Part of the DNA SAC program is the development and application of advanced finite-difference codes to improve calculations on grout flow along a tunnel. A dynamic grout extrusion experiment[5] was developed to provide results for code validation.

Figures 1 and 2 show the extrusion apparatus in which a cylindrical specimen of superlean grout (SLG) in a steel container is driven into a concentric tunnel in a Lucite cylinder by a steel piston. The energy source is a charge of low pressure explosive consisting of an 80/20 mixture by weight of PETN powder and plastic microballoons. The gaseous detonation products pass through holes in two baffle plates to fill an expansion chamber. The resulting pressure acts on a diaphragm and is transmitted to the piston through a layer of oil. With this loading assembly design, innumerable pulse shapes can be obtained having a fairly smooth rise and a very smooth decay.

Instrumentation consists of a high-speed camera that records the SLG surface displacement along the tunnel in the Lucite. This camera also records the piston displacement by observing piston extension rods that move along fixed scales in the camera view. Figure 3 shows typical frames taken from the high-speed camera film of a development test. Two pressure transducers record the pressure in the oil that transmits the

explosive gas pressure to the piston. Small colored ceramic beads were cast in the grout for pretest and posttest displacement assessment to supplement the instrumentation data.

The SLG, designated HSSL-1A because it is made with the formula for HSSL-1, is a grout with well characterized material properties[2] (Figure 4); 14-day aging was selected.

Figures 5 and 6 show the two SLG containers used in the experiments. These containers serve as molds for SLG pouring and aging and as nozzles for the extrusion process.

In typical experiments, 35 grams of explosive mixture produced piston pulses with maximum pressures of 600 to 900 psi, times to reach maximum pressures from 4 to 6 msec, and durations greater than 14 msec. Grout surface displacements in 1-1/2-inch-diameter tunnels ranged from 3 inches in 11 msec to 4 inches in 13 msec. Maximum surface velocities ranged from 25 to 45 feet/sec. Results are presented in Section III.

An unknown in the extrusion experiments is the shear stress at the steel boundary of the grout caused by friction between the grout and steel or, in the case of no relative interface motion, local shear stress flow. To provide friction data, an experiment was devised that consists of measuring the resistance of a SLG piston to motion along a steel cylinder. Figure 7 shows the SLG piston held between two short steel pistons that are connected to each other by a central steel rod. Before this composite piston is projected along the steel cylinder, the SLG is subjected to pressure by rotating one steel piston on the threaded rod. The pressure is calculated from circumferential strain gage or diameter change readings along the cylinder. The composite piston is attached to the piston of the extrusion apparatus of Figures 1 and 2 after removing the extrusion portion of the assembly. The pressure applied to the piston and the resulting motion are recorded and the friction force determined from the simple equation of motion.

B. Containment Experiments

A laboratory experiment[6] was devised and developed to investigate the effect of a residual stress field on containment. The first objective of this experiment is to demonstrate that a residual stress field exists around an exploded cavity. The second objective is to establish the extent to which the residual stress field aids containment. The experiment is shown schematically in Figure 8. A small spherical explosive charge representing the nuclear device is sealed and cast in a much larger sphere of grout with properties similar to those of Nevada Test Site tuff (Figure 8a). The grout surface is sealed and hydraulically pressurized to represent overburden (Figure 8b). The explosive is detonated and the residual gases are released (Figure 8c). Fluid is pumped into the cavity at a constant flow rate until fracture causes equalization of internal and external pressures (Figure 8d).

The final stages of gas release and cavity pressurization are included to determine the effect of the residual stress field by comparing the cavity pressure required to crack the RMG sphere with and without residual stresses. In the experiments without a residual stress field, spherical cavities are cast in the grout spheres; the cavities are the same size as the exploded cavities.

Figure 9 shows a 12-inch-diameter RMG sphere inside a steel vessel containing water under pressure. The sphere is suspended from the lid by a threaded steel tube cast in the grout; the tube is used also to position the charge, to guide the detonator cables, and to drill into the cavity after detonation. The water pressure in the vessel was maintained constant (1000 psi) throughout the test series by incorporating a high-pressure gas reservoir and valve in the water supply line.

Figure 10 shows the constant flow rate system. The specifications are listed in Table 1. The motor shaft rotates at a constant angular velocity (6 rpm). A slotted tubular coupling allows an extension of the shaft to translate as well as to rotate. The shaft extension is threaded and rotates in a fixed threaded bearing causing constant velocity translation of the pump piston. Hence, fluid is driven at a constant rate into

the cavity supply line (Figure 9). Fluid flow is recorded automatically with pen and chart by measuring the voltage change across an angular potentiometer geared to the rotating shaft; chart speed introduces time, and calibration test results relate voltage change to flow (11.2 cm^3/volt). Similarly, pressure is recorded by measuring the voltage change across a calibrated electrical resistance pressure transducer.

Figure 11 shows the explosive charge used in all but two early tests. It contains 1 gram of PETN. The charge has to be carefully sealed against water in the surrounding grout being squeezed between the spherical container and the bridge plug to soak the PETN and prevent detonation. In future charge designs, the amount of inert material, especially the bridge plug, should be reduced to improve spherical symmetry.[9]

Figures 12 and 13 show properties of the rock matching grout used in the experiments.

C. Simple Containment Analysis

A simple containment analysis[7] was performed to aid in understanding the mechanics of dynamic cavity expansion and to supplement similar work that has been done by computer codes. In the formulation, a gas with a known equation of state is assumed to instantaneously pressurize a spherical cavity in a solid homogeneous and isotropic medium. A simple analytical treatment of the subsequent cavity expansion was made possible by idealization of the following material properties:

- Incompressibility
- Elastic-perfectly plastic behavior
- Yielding according to the Mises condition
- Plastic straining according to the associated flow rule.

Overburden is included as a constant pressure infinitely far from the cavity.

The gas pressure causes cavity expansion and creates a distribution of outward radial particle velocity in the medium. As expansion proceeds, the gas pressure decays and the tensile tangential stresses increase to

slow down expansion and eventually cause rebound of the medium. Subsequent, relatively small amplitude oscillations occur until the kinetic energy is dissipated; in the analysis, the energy dissipates only by plastic work of distortion. During expansion and contraction, plastic zones spread out from the cavity and greatly influence the character of the stress fields. The highly compressive character of the residual stress field takes shape during the rebound.

The analysis is presented in SRI Topical Report 3702-2 (Reference 7). Conclusions based on the analysis are given in Section V.

Table 1

HYDROFRACTURE SYSTEM SPECIFICATIONS

Motor:	Dayton Gear motor model 5K933 1/4 HP, 6 rpm, 600 in-lb torque
Pump:	High Pressure Equipment Co. Model 87-6-5 60 cm^3 capacity, 5000 psi maximum pressure 4.26 cm^3/min. flow rate (0.71 cm^3/revolution)
System:	Fluid: Dyed Glycerin Volume (excluding pump) 31.33 cm^3.

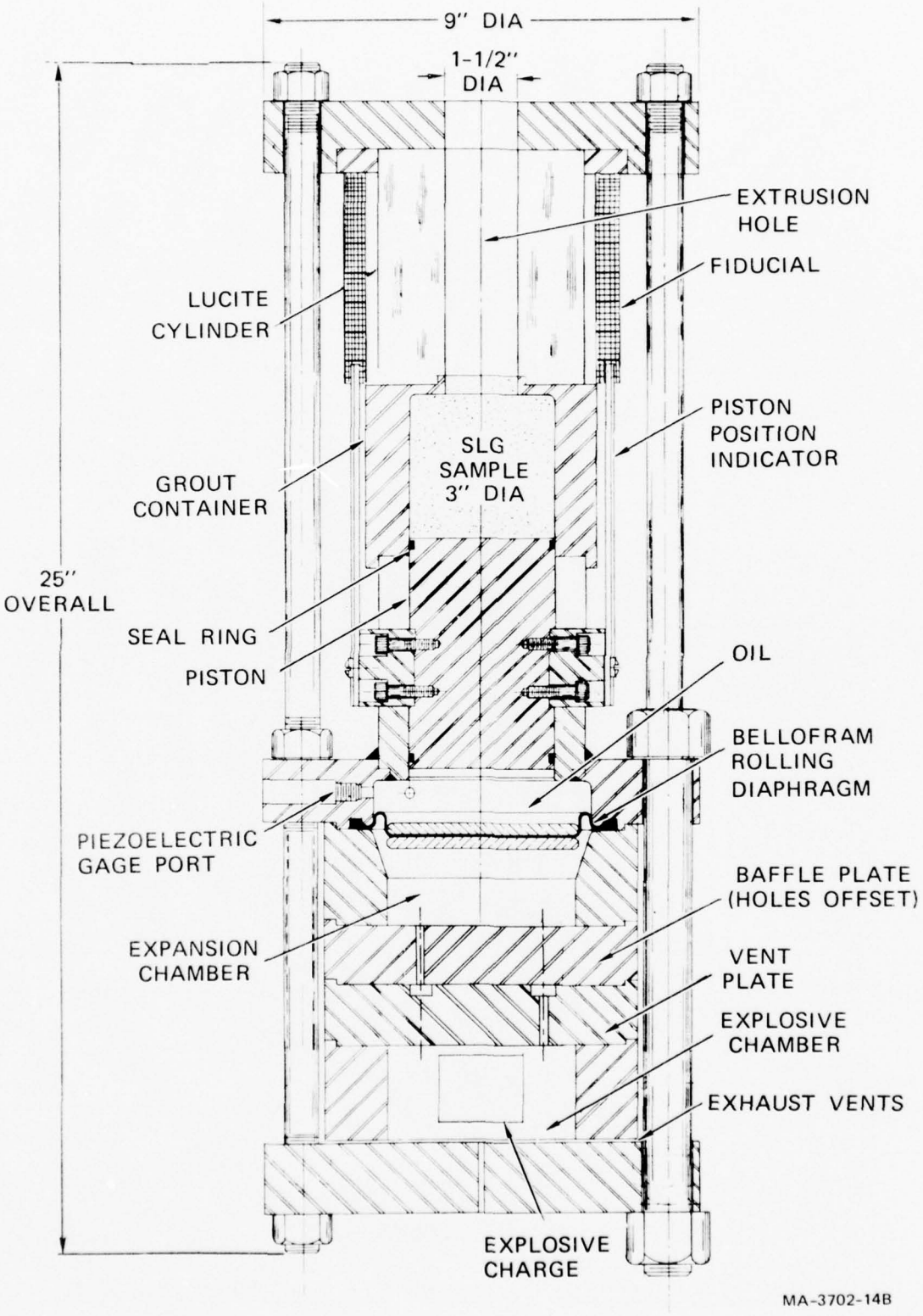

FIGURE 1 PISTON-DRIVEN EXTRUSION APPARATUS

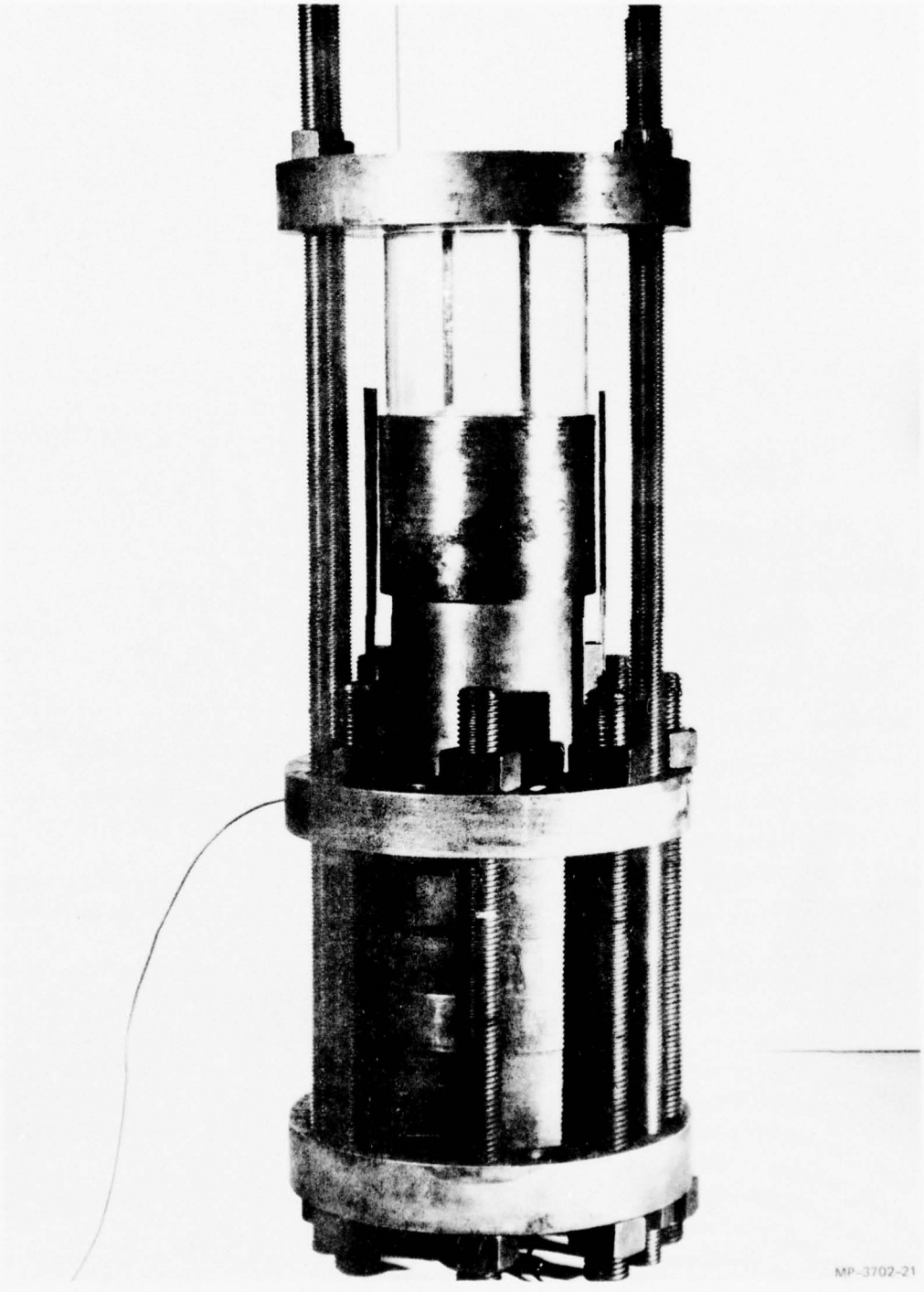

FIGURE 2 PHOTOGRAPH OF AXIALLY DRIVEN SLG EXTRUSION APPARATUS

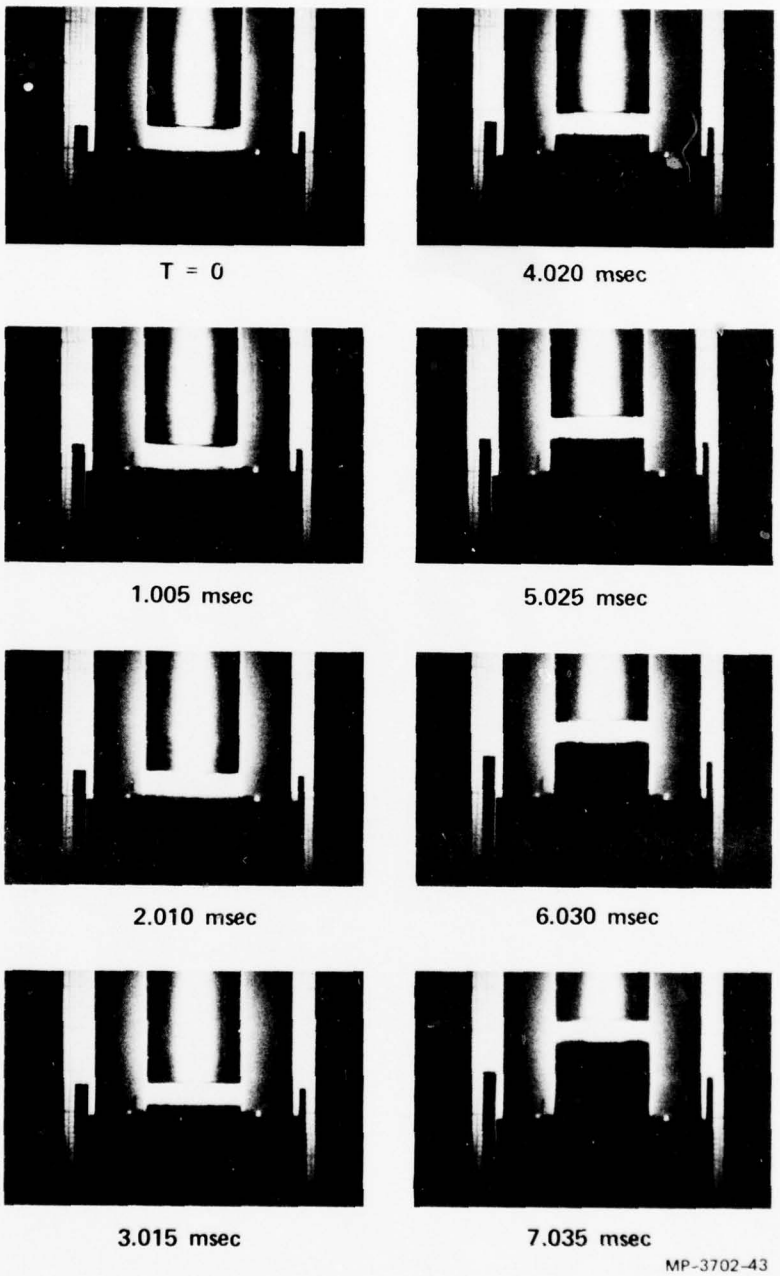

FIGURE 3 DYNAMIC EXTRUSION OF AXIALLY DRIVEN SLG (TEST 102)

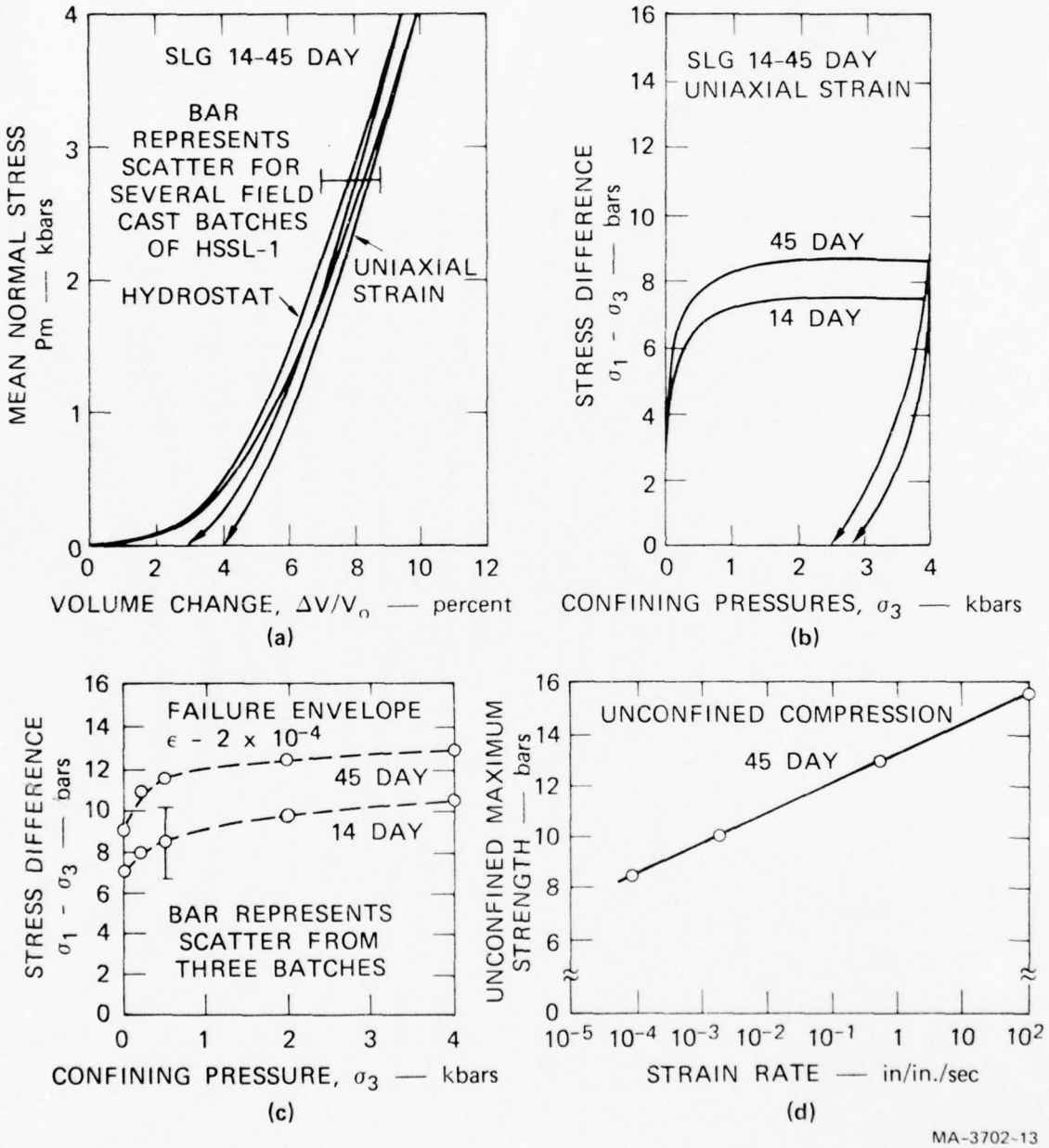

FIGURE 4 PROPERTIES OF HSSL-1

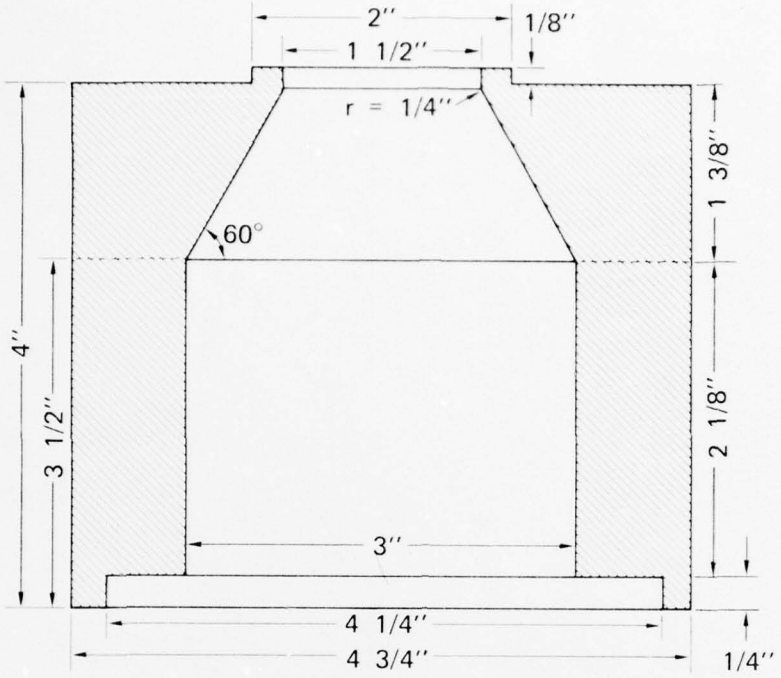

FIGURE 5 CONICAL-CYLINDRICAL MOLD FOR SLG SPECIMEN

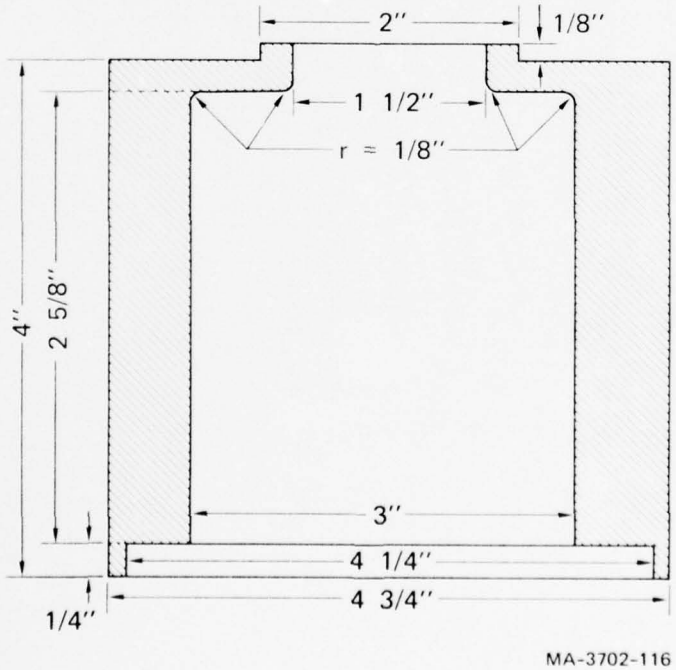

FIGURE 6 CYLINDRICAL MOLD FOR SLG SPECIMEN

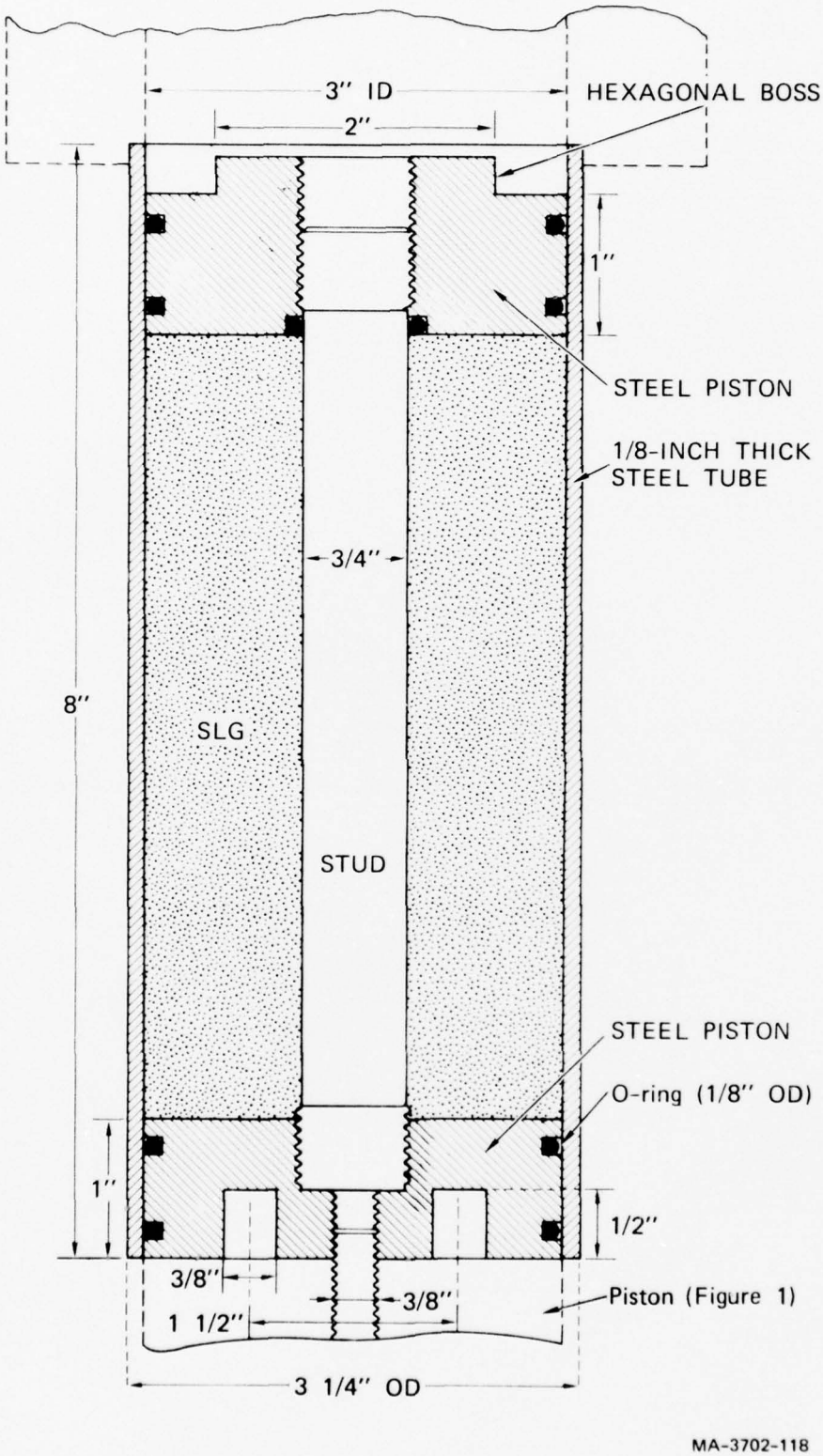

FIGURE 7 COMPOSITE PISTON FOR DYNAMIC FRICTION MEASUREMENTS

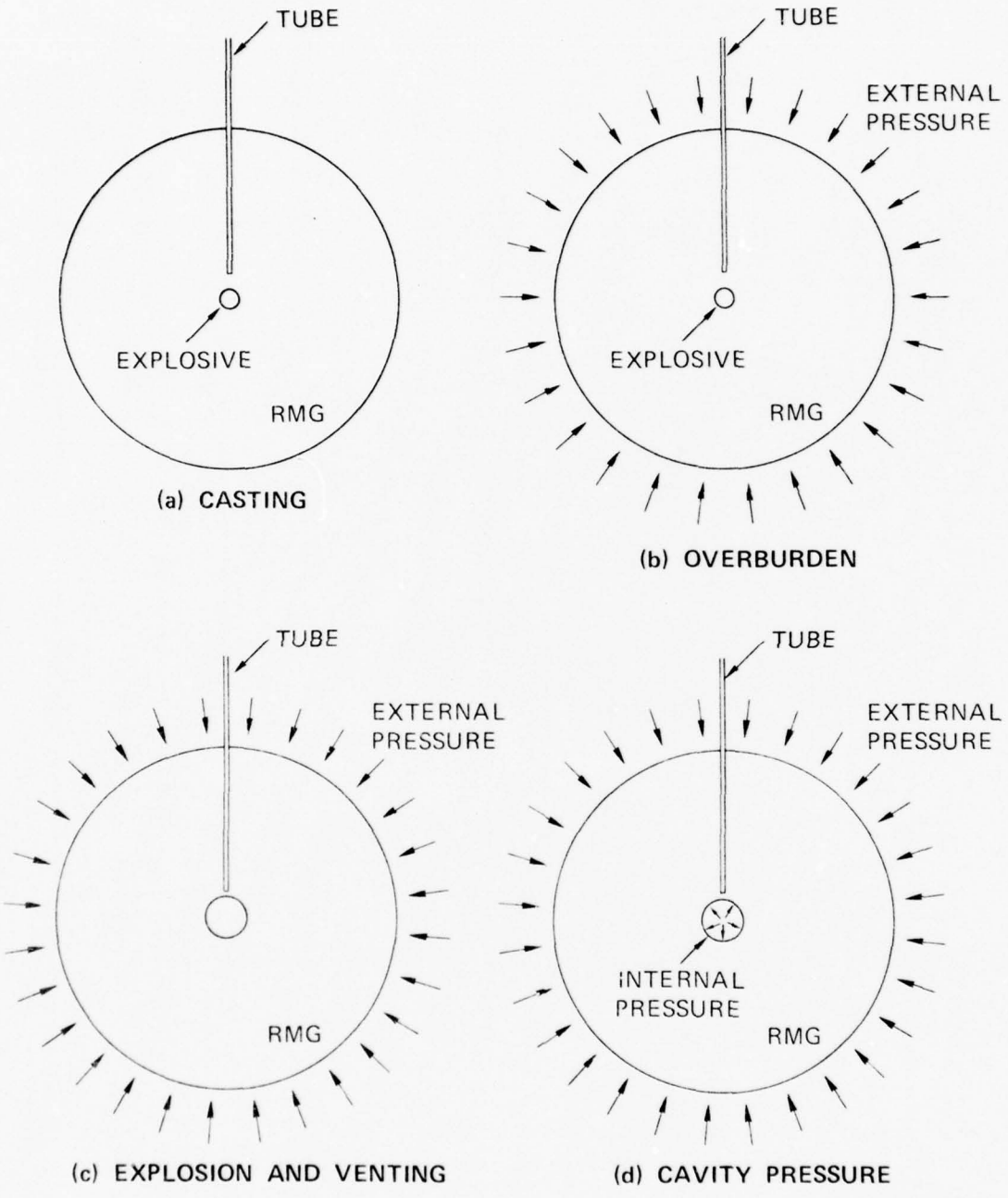

FIGURE 8 SEQUENCE OF OPERATIONS IN CONTAINMENT EXPERIMENT

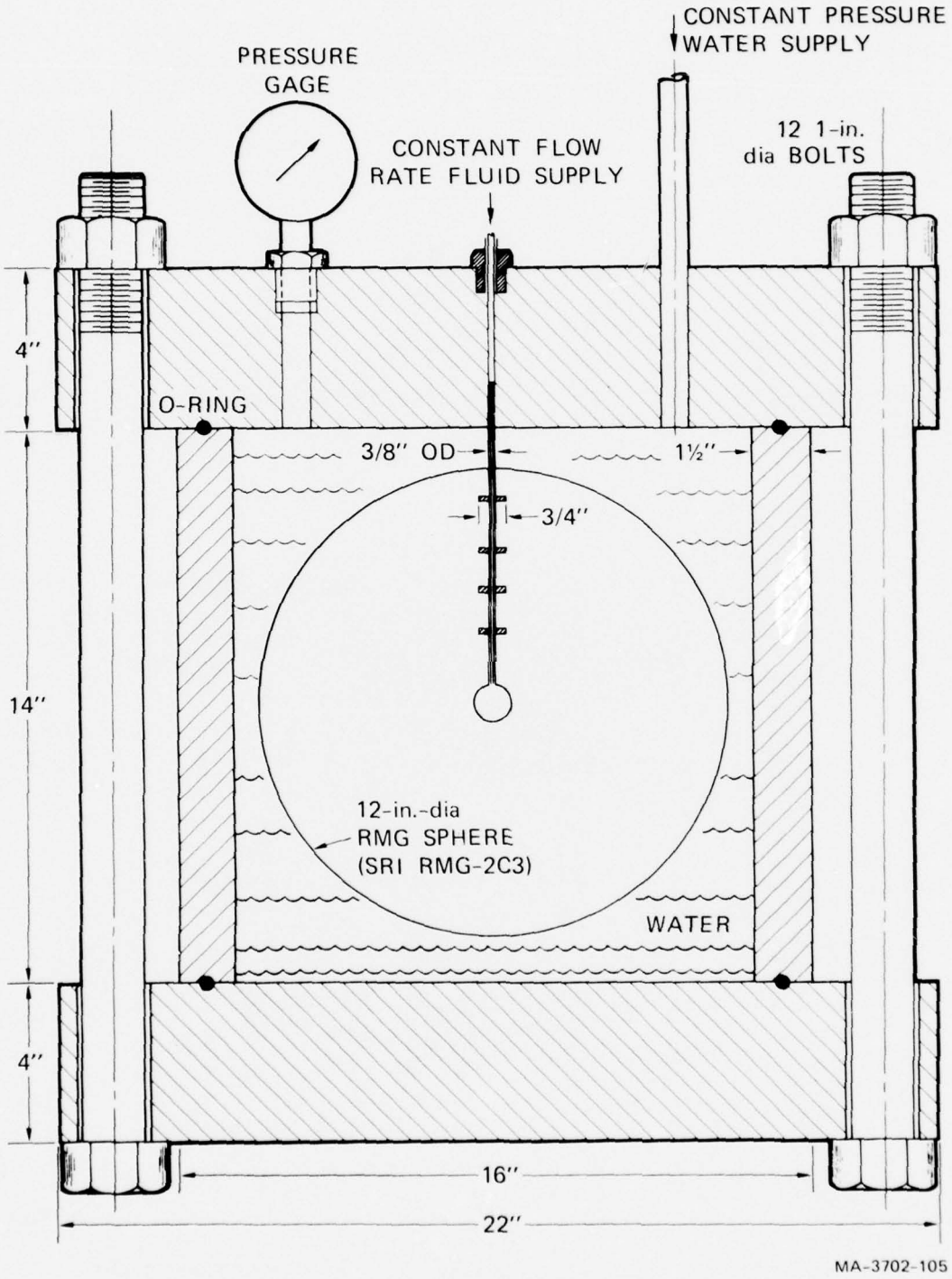

FIGURE 9 CONTAINMENT EXPERIMENT APPARATUS

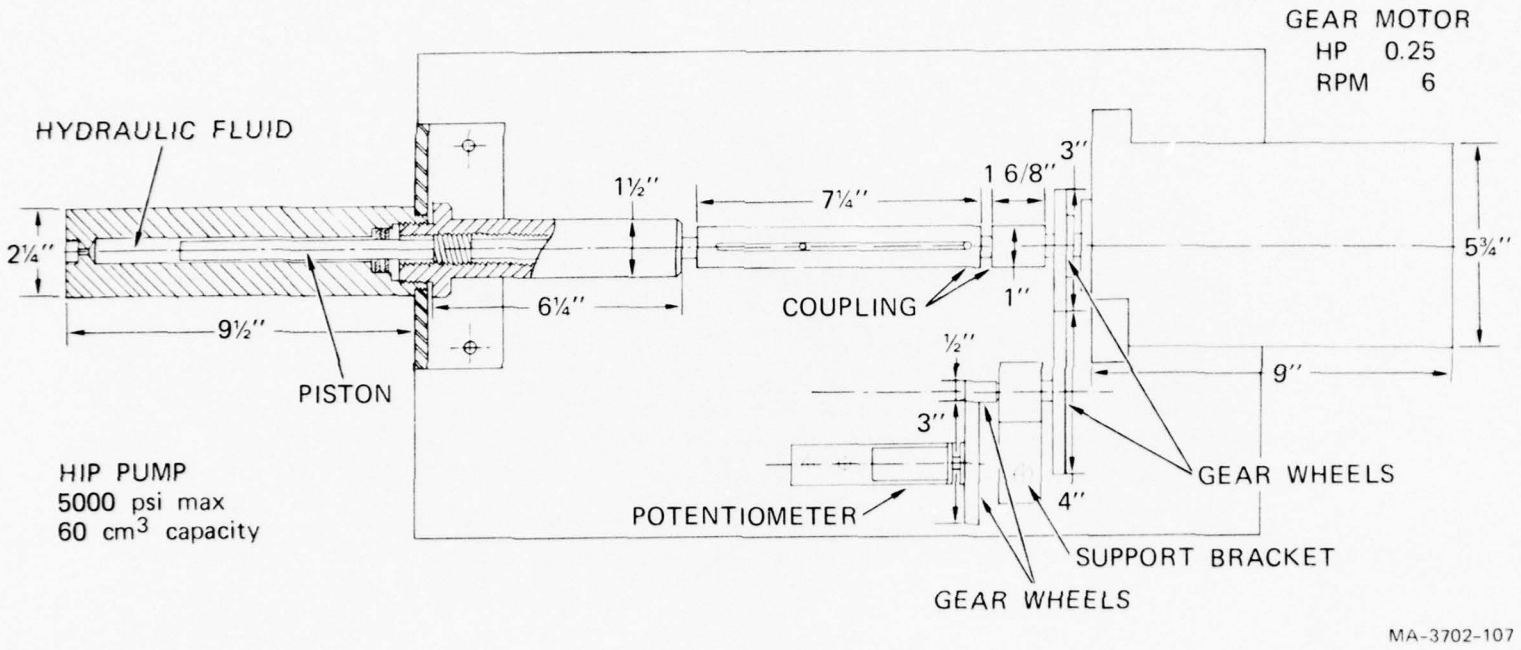

FIGURE 10 CONSTANT FLOW-RATE HYDROFRACTURE SYSTEM

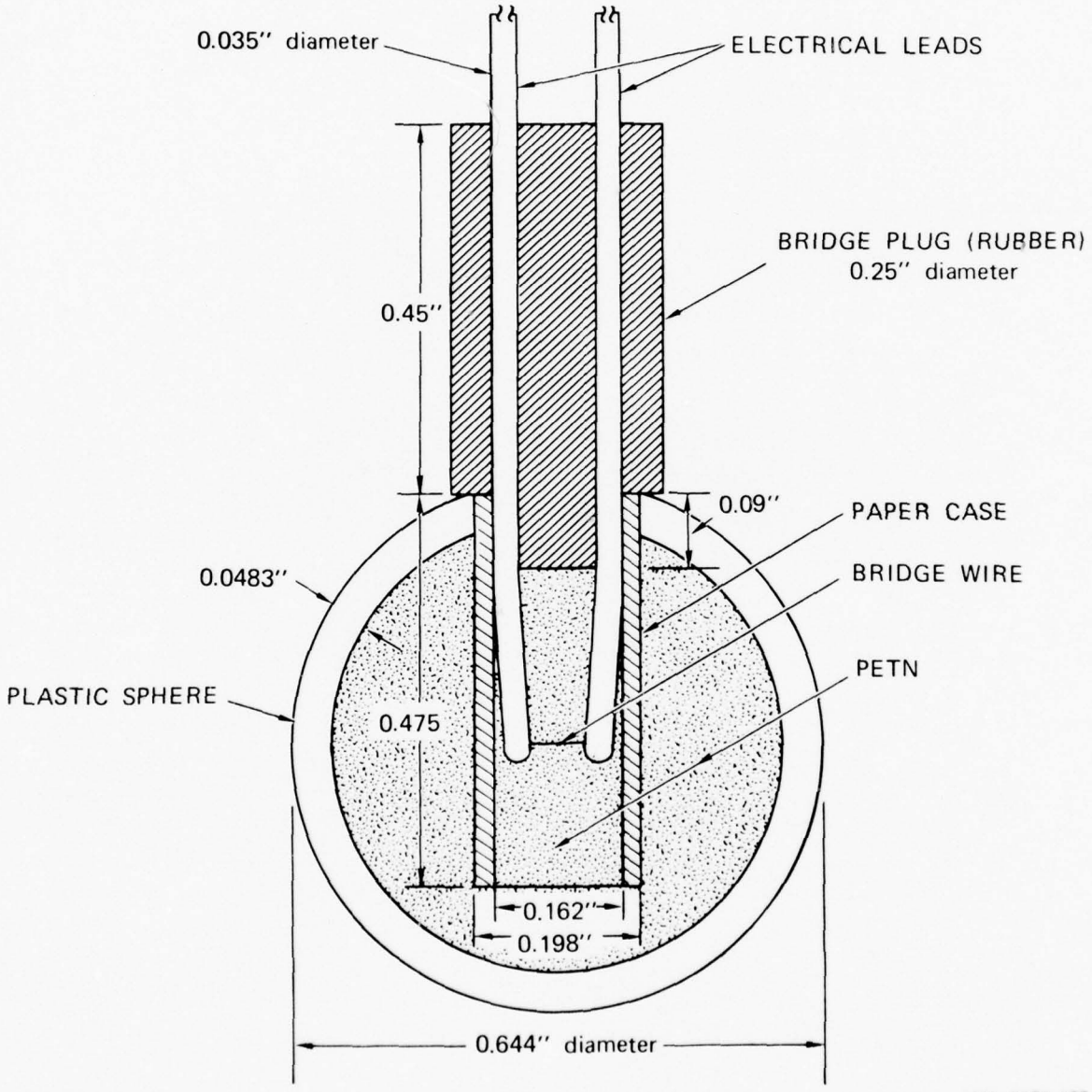

FIGURE 11 EXPLOSIVE CHARGE DETAILS

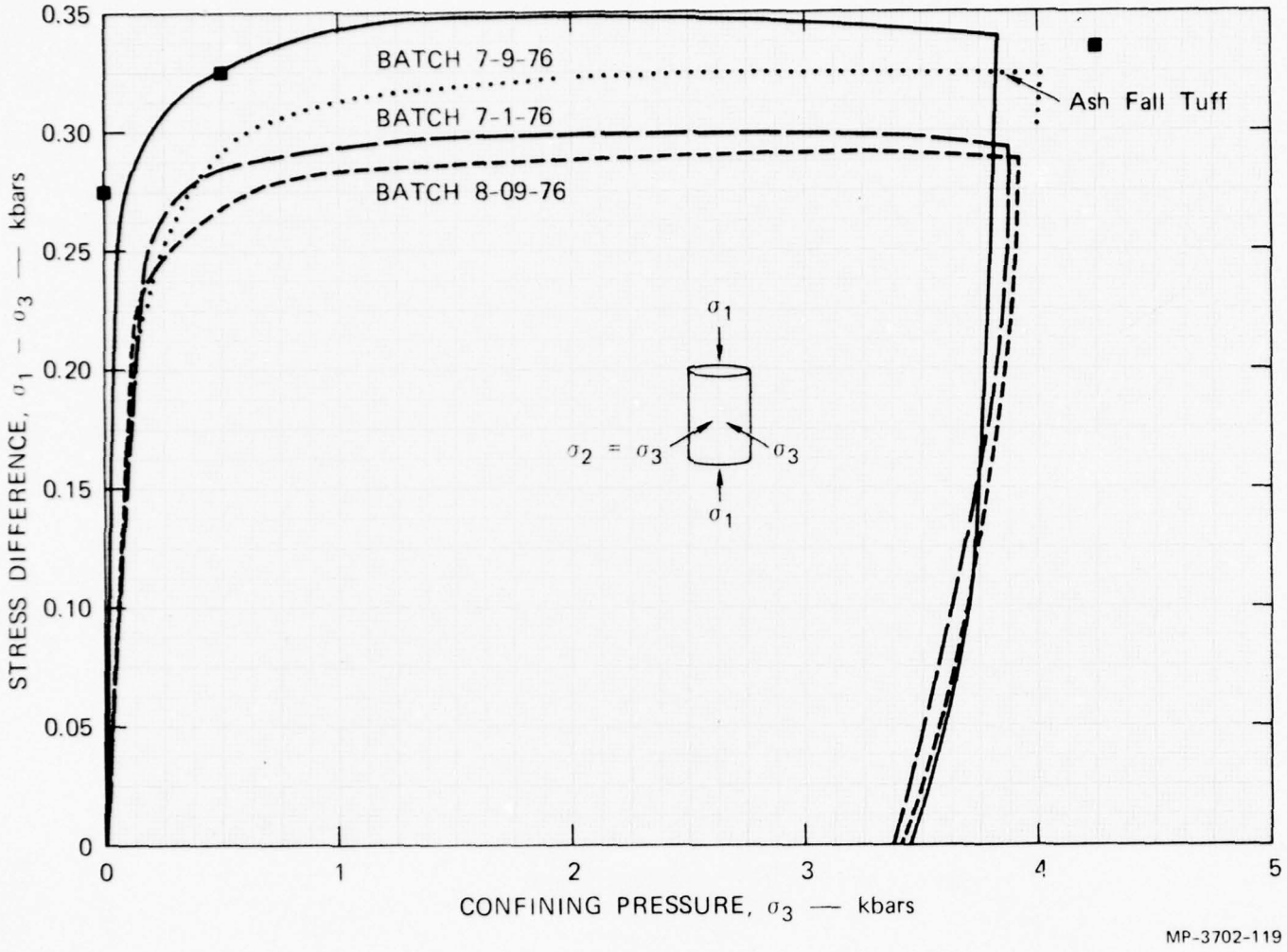

FIGURE 12 STRENGTH PROPERTIES OF THE ROCK-MATCHING GROUT SRIRMG-2C3

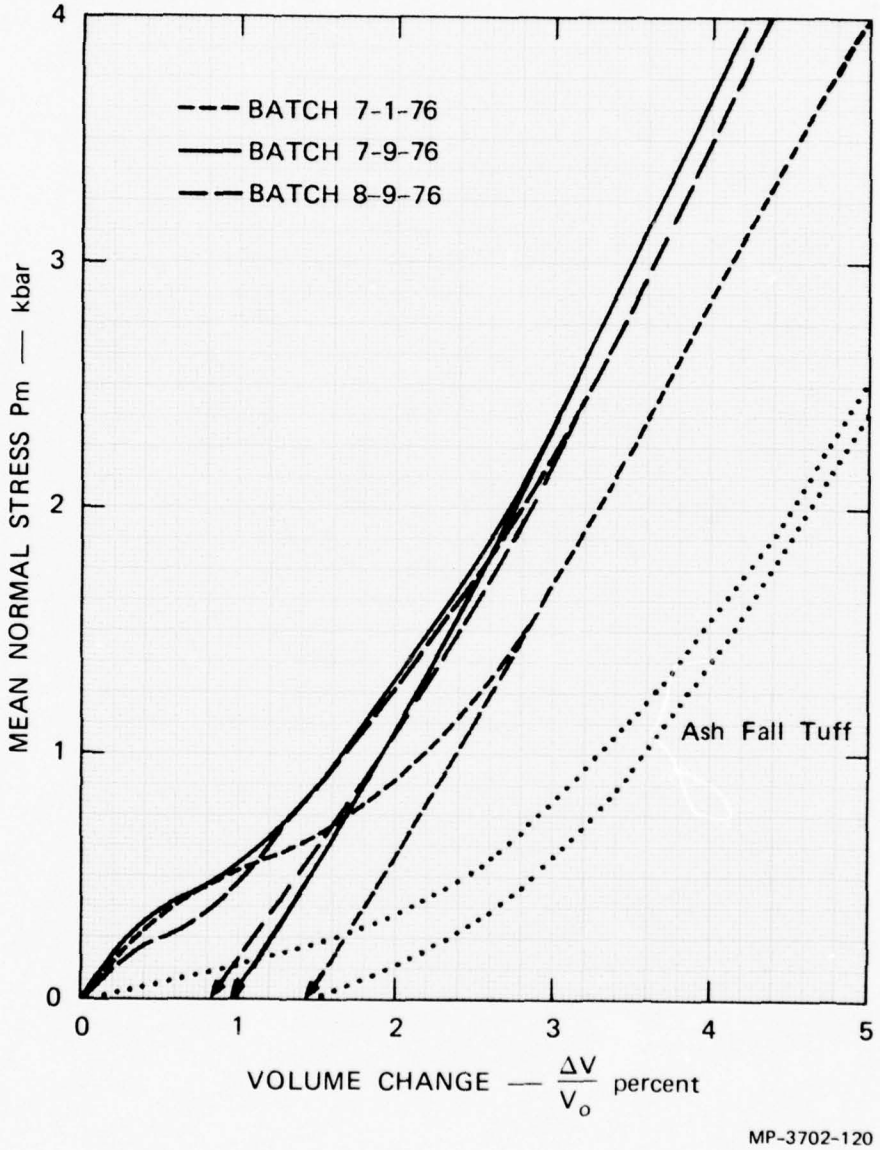

FIGURE 13 STRENGTH PROPERTIES OF THE ROCK-MATCHING GROUT SRI RMG-2C3

III EXTRUSION EXPERIMENTAL RESULTS

A. Extrusion Experiments

Table 2 shows the organization of the data for six dynamic extrusion tests arranged in three groups of two tests. Groups 1 and 2 have the same cone-cylinder configuration (Figure 5), different piston pressures (Figure 14), and grout from different batches (Table 5). Group 3 has the cylindrical configuration (Figure 6), piston pressures comparable to those of Group 2 (Figure 14), and grout from the same batch as Group 2 (Table 5).

Figures 14 and 15 show the group average piston pressures and impulses, and Figure 16 and 17 show the group average SLG front and piston displacements. Two transducers monitored the pressure in each test. The two pressure records were averaged to provide the test average pressure. In each group, the two test average pressures were averaged to provide the group average pressure.

Figures 18 to 29 present the results by groups to allow a comparison of the two test results in each group. The pressures and impulses being compared are test averages.

Tables 3 and 4 give the initial and final locations of particles (colored ceramic beads) cast in the grout. Figures 30 and 31 explain the XY coordinate system and show diagrams of the particle locations and sample shapes.

B. Friction Experiments

Tests 111 and 121 were performed to obtain the friction between the SLG and the steel container. In both tests, the SLG in the steel tube (Figure 7) was squeezed between the two steel end plates to a pressure of 1000 psi. Figures 32 and 33 show the pressure pulses applied to the

piston in Tests 111 and 121, and Figures 34 and 35 show the resulting piston displacements.

The equation of piston motion is

$$pA = M\frac{d^2x}{dt^2} + fS \qquad (1)$$

where

p = pressure applied to the piston (Figures 32 and 33)
A = piston area (45.6 cm^3)
M = piston mass (7808 grams)
x = piston displacement (Figures 34 and 35)
f = friction
S = surface area between steel and SLG (361.3 cm^3)

The friction results of Figure 36 were determined by using a fifth degree polynomial for a least squares fit of the x-t data to determine the piston acceleration in Equation (1). Approximate averages are 2-1/2 and 3 bars (36 and 43 psi); a fourth degree polynomial gave the same results. A useful addition to the experiment would be an accelerometer attached to the piston to attempt to measure directly the acceleration required in Equation (1).

C. Properties of SLG

Table 5 gives SLG properties obtained from batch samples. Results for Tests 158 and 159 are included because the samples experienced negligible extrusion under Group 2 loading and sample configuration (same as Tests 140 and 141). The slightly higher crush strength implies proximity to the threshold of extrusion. Figures 37 and 38 show strength properties determined by Terra Tek from samples of the grout batch for Tests 158 and 159.

The main improvement required in the extrusion experiment is a reduction in scatter of the SLG properties. Table 5 shows that for the HSSL-1A mixture of Table 6, unconfined crush strengths can vary from 124 to 174 psi

even with precise weighings with dried fines, same mixing times, careful sealing, and same aging periods and temperatures. Because of the small batches required for the samples, a sieve analysis was conducted on six samples of the Nevada Test Site fines. The results are listed in Table 7 and are indicated by the bars in Figure 39. Three particle size distributions were prepared, according to Table 8 and the points in Figure 39, and used in the HSSL-1A mixture of Table 6. After 14 day aging, the samples were subjected to unconfined crush tests. Results are given in Table 8. Although the tests are limited in number, the strengths exhibit a trend with reduced scatter. It is recommended that design size distributions be incorporated in future extrusion tests if further strength tests consolidate the findings in Table 8.

Table 2

ORGANIZATION OF SLG EXTRUSION DATA[a]

Group	Test	SLG Configuration	Figure Number					Table
			Piston Press.	Piston Impulse	SLG Displ.	Piston Displ.	Particle Displ.	Particle Displ.
1	134 135	Cone-cylinder (Figure 5)	14,18	15,19	16,20	17,21	30 31	3
2	140 141	Cone-cylinder (Figure 5)	14,22	15,23	16,24	17,25	--	3
3	142 143	Cylinder (Figure 6)	14,26	15,27	16,28	17,29	--	4

[a]Technical Report TR 76-3702-4 (Reference 5) contains the complete data.

Table 3

PARTICLE LOCATIONS BEFORE AND AFTER EXTRUSION

BEFORE	COORDINATES AFTER EXTRUSION[a]											
X = 0	TEST 134			TEST 135			TEST 140			TEST 141		
X = 0.5	X = 0	X = 0.5 before		X = 0	X = 0.5 before		X = 0	X = 0.5 before		X = 0	X = 0.5 before	
Y	Y	X	Y	Y	X	Y	Y	X	Y	Y	X	Y
3.63[b]	7.43[b]			7.34[b]			7.29[b]			7.20[b]		
3.13	6.93	0.46	6.93	6.84	0.49	6.84	6.79	0.50	6.79	6.70	0.46	6.70
2.63	6.22	0.34	6.14	6.16	0.37	6.05	6.17	0.40	6.04	6.03	0.35	5.92
2.13	4.68	0.25	4.80	4.59	0.23	4.73	4.90	0.29	4.75	4.49	0.23	4.56
1.63	2.67	0.31	2.74	2.66	0.33	2.61	2.78	0.38	2.77	2.49	0.31	2.55
1.13	2.00	0.43	2.02	2.07	0.45	2.02	2.05	0.50	2.02	2.06	0.50	2.08
0[c]	0.90[c]			0.90[c]			0.92[c]			0.93[c]		

[a]Coordinates of embedded ceramic beads

[b]SLG top surface

[c]Piston-SLG interface

Table 4

PARTICLE LOCATION BEFORE AND AFTER EXTRUSION

BEFORE	COORDINATES AFTER EXTRUSION[a]					
X = 0	TEST 142			TEST 143		
X = 0.5	X = 0	X = 0.5 before		X = 0	X = 0.5 before	
Y	Y	X	Y	Y	X	Y
3.56[b]				6.20[b]		
3.06	6.55	0.50	6.55	5.70	0.50	5.70
2.56				5.11	0.22	5.33
2.06	3.00	0.39	2.92	2.79	0.38	2.96
1.56	2.34		2.32	2.19	0.41	2.23
1.06	1.81	0.50	1.81	1.68	0.44	1.72
0[c]	0.82[c]			0.67[c]		

[a]Coordinates of embedded ceramic beads

[b]SLG top surface

[c]Piston-SLG interface

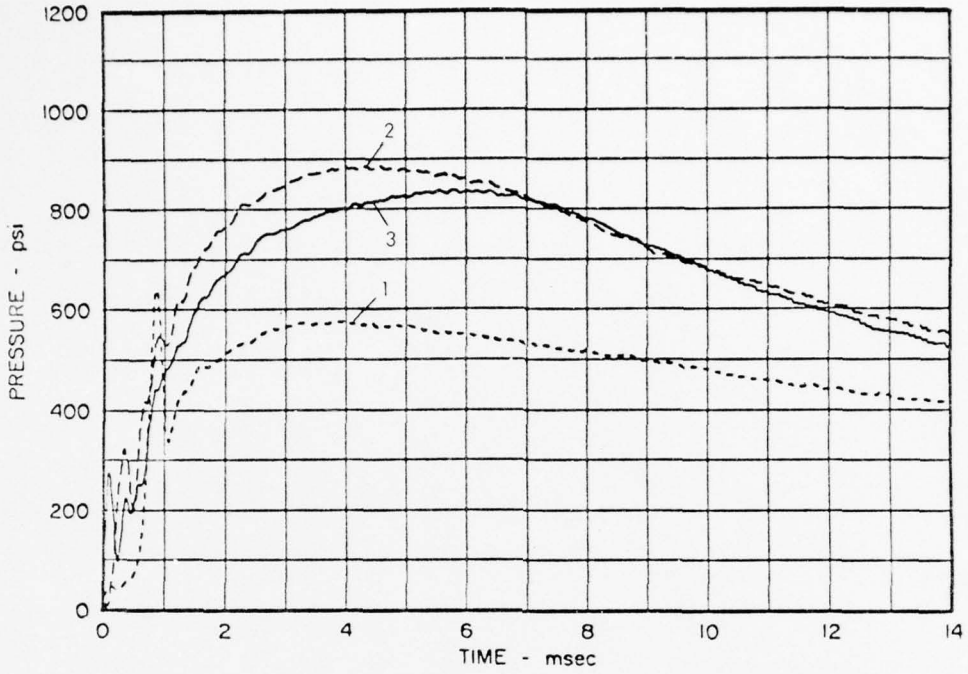

FIGURE 14 PRESSURE PULSE AVERAGES FOR TEST GROUPS 1, 2, AND 3

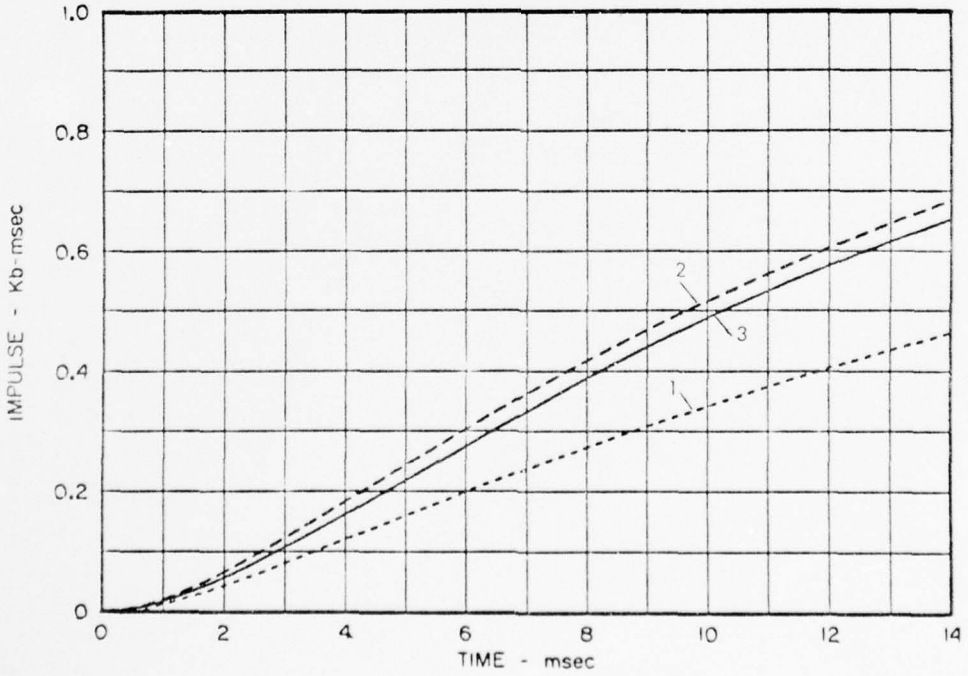

FIGURE 15 IMPULSE AVERAGES FOR TEST GROUPS 1, 2, AND 3

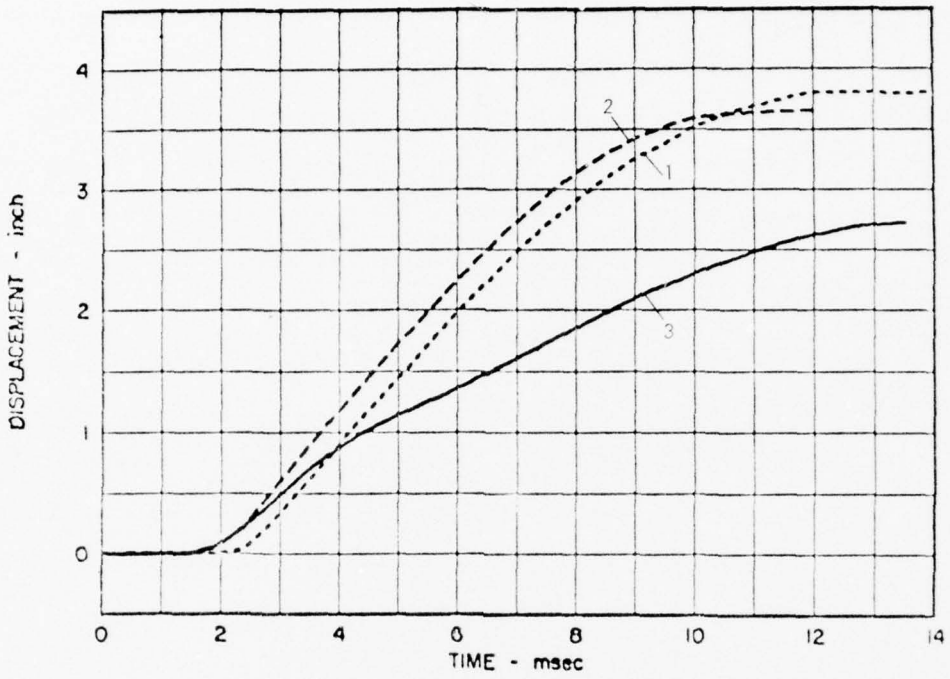

FIGURE 16 SLG FRONT DISPLACEMENT AVERAGES FOR TEST GROUPS 1, 2, AND 3

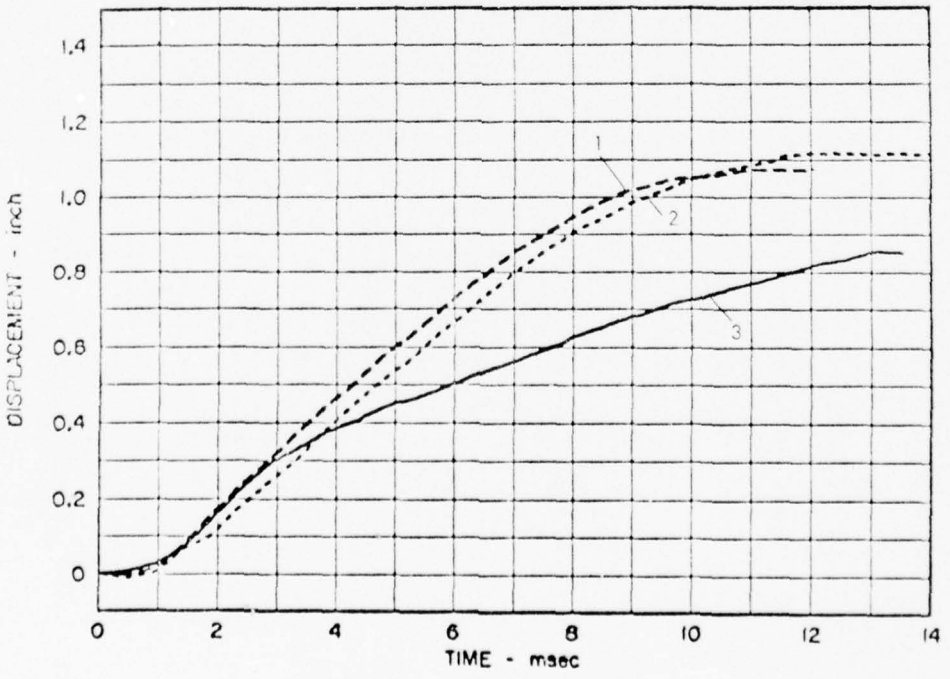

FIGURE 17 PISTON DISPLACEMENT AVERAGES FOR TEST GROUPS 1, 2, AND 3

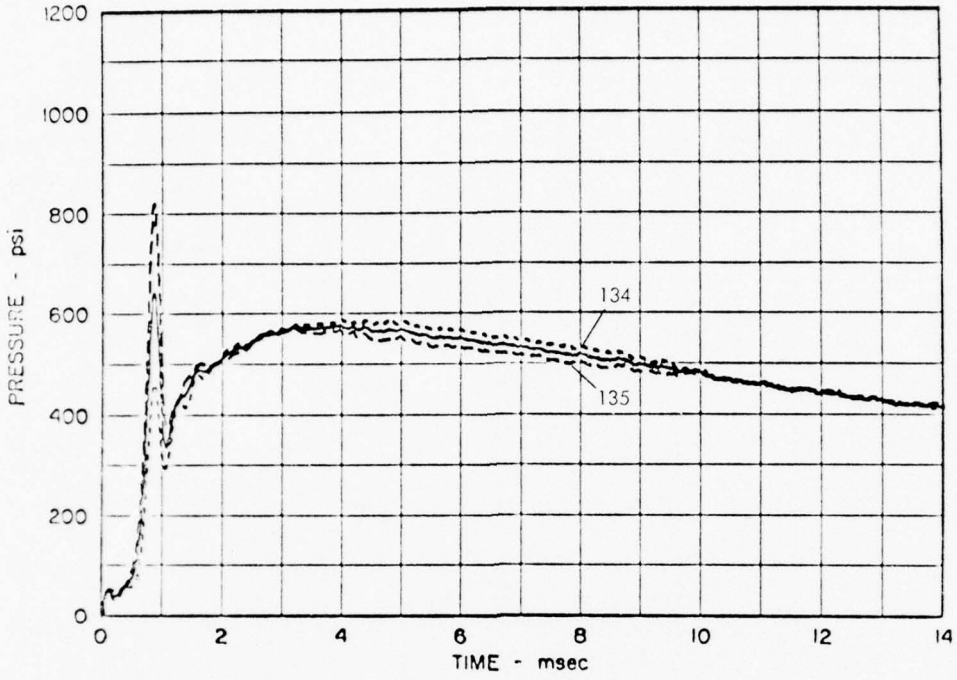

FIGURE 18 PRESSURE PULSES FROM GROUP 1 TESTS 134 AND 135

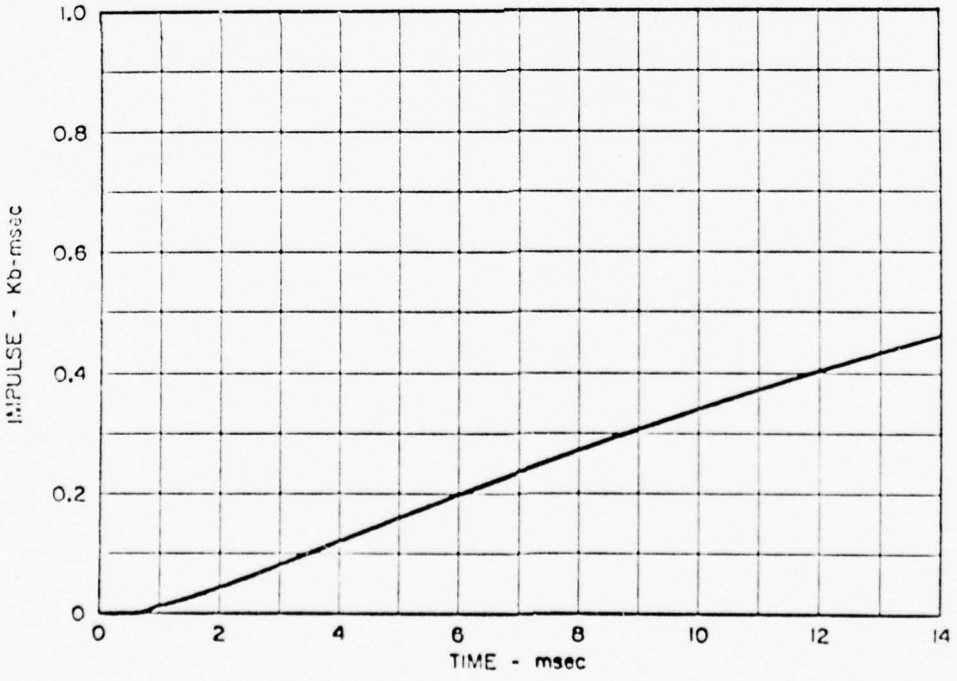

FIGURE 19 IMPULSES FROM GROUP 1 TESTS 134 AND 135

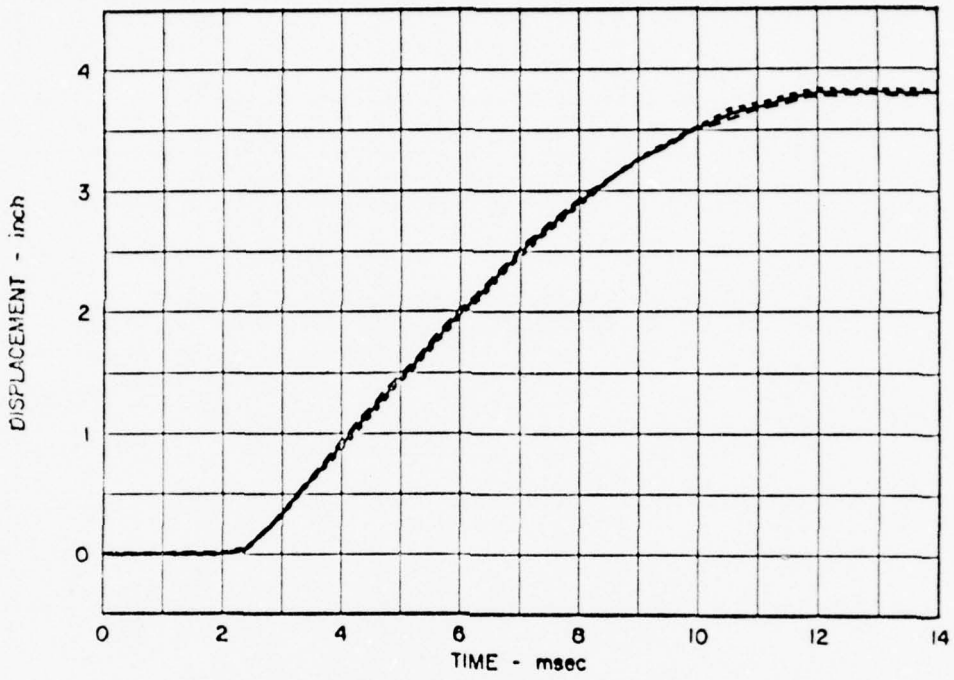

FIGURE 20 SLG FRONT DISPLACEMENTS FROM GROUP 1 TESTS 134 AND 135

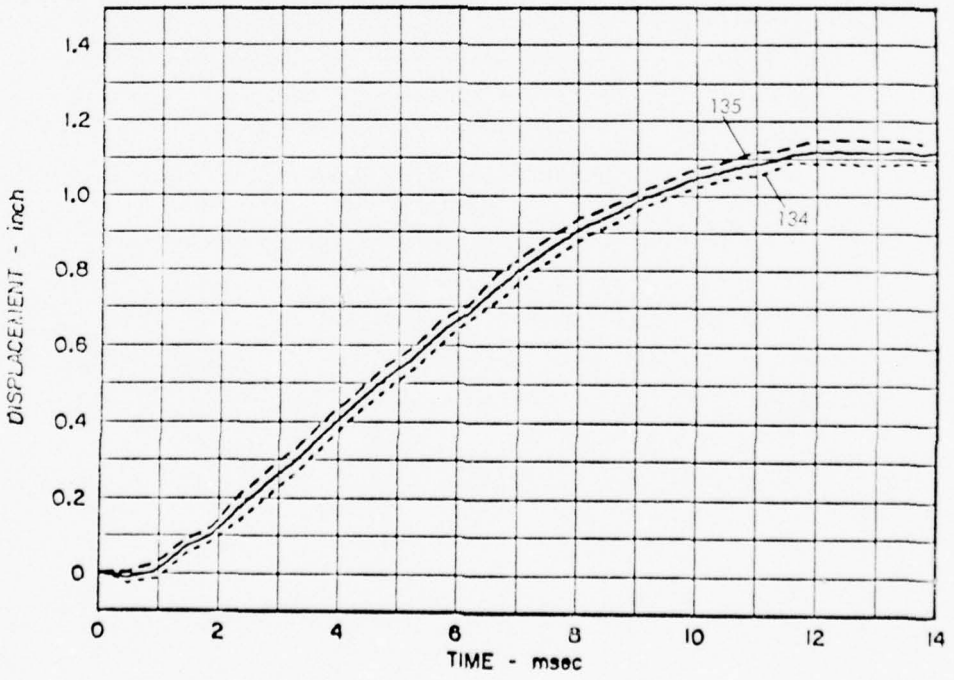

FIGURE 21 PISTON DISPLACEMENTS FROM GROUP 1 TESTS 134 AND 135

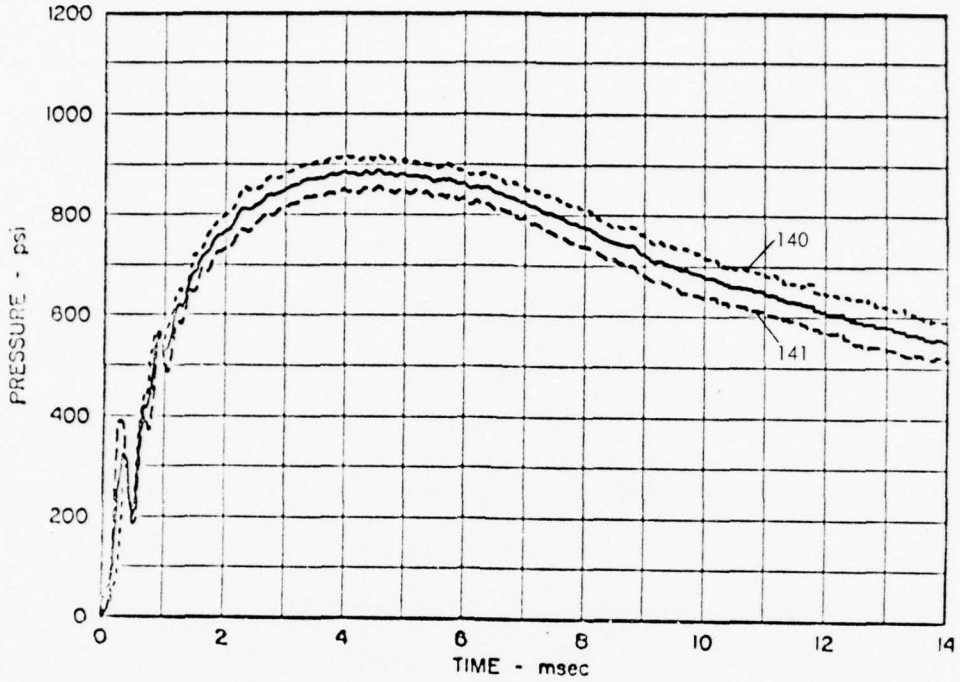

FIGURE 22 PRESSURE PULSES FROM GROUP 2 TESTS 140 AND 141

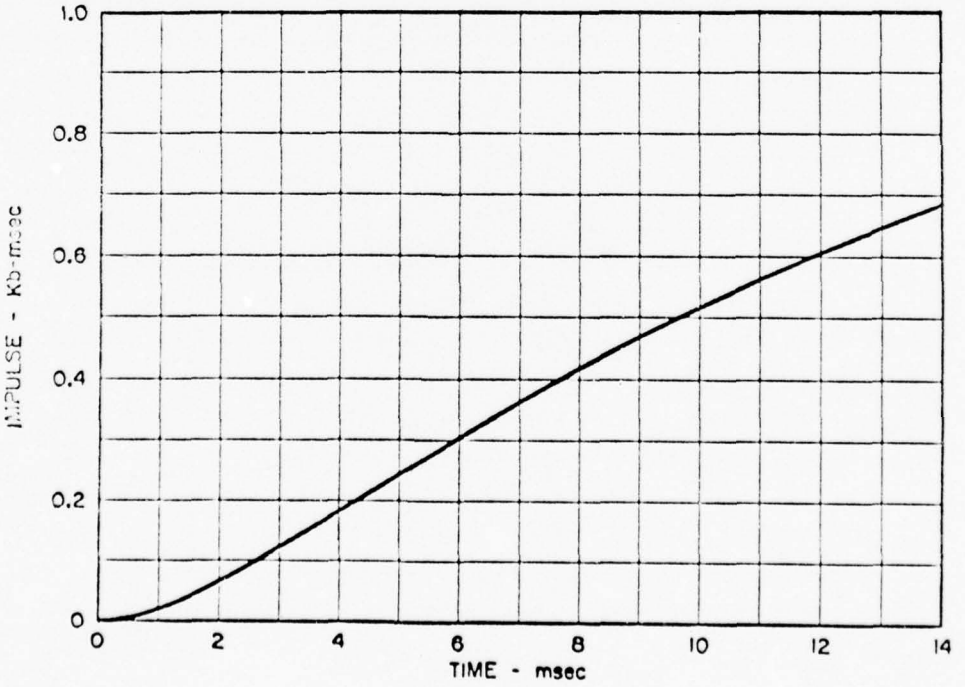

FIGURE 23 IMPULSES FROM GROUP 2 TESTS 140 AND 141

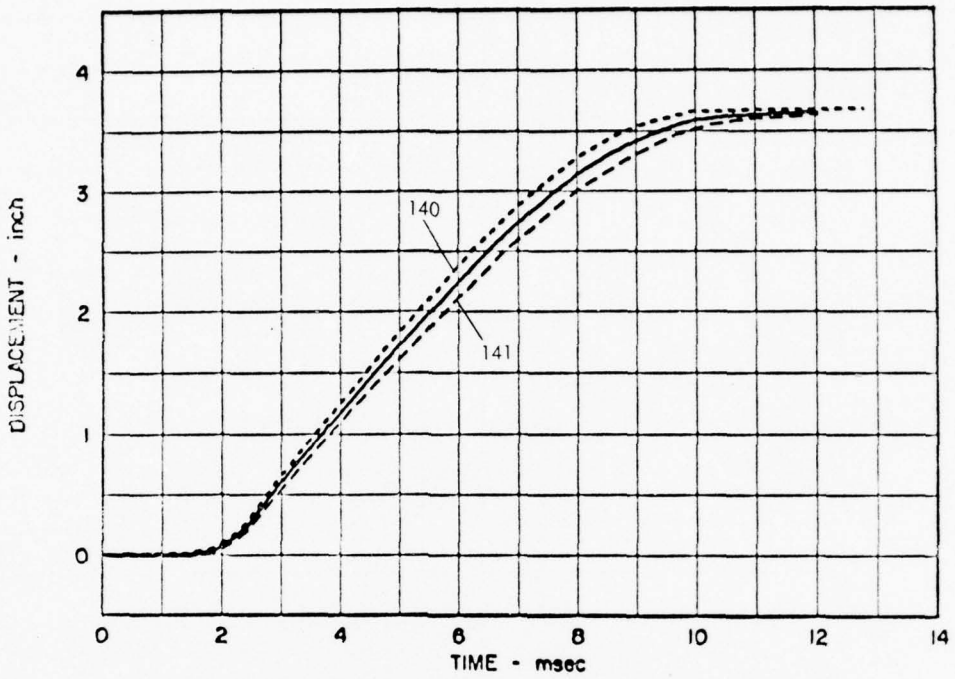

FIGURE 24 SLG FRONT DISPLACEMENTS FROM GROUP 2 TESTS 140 AND 141

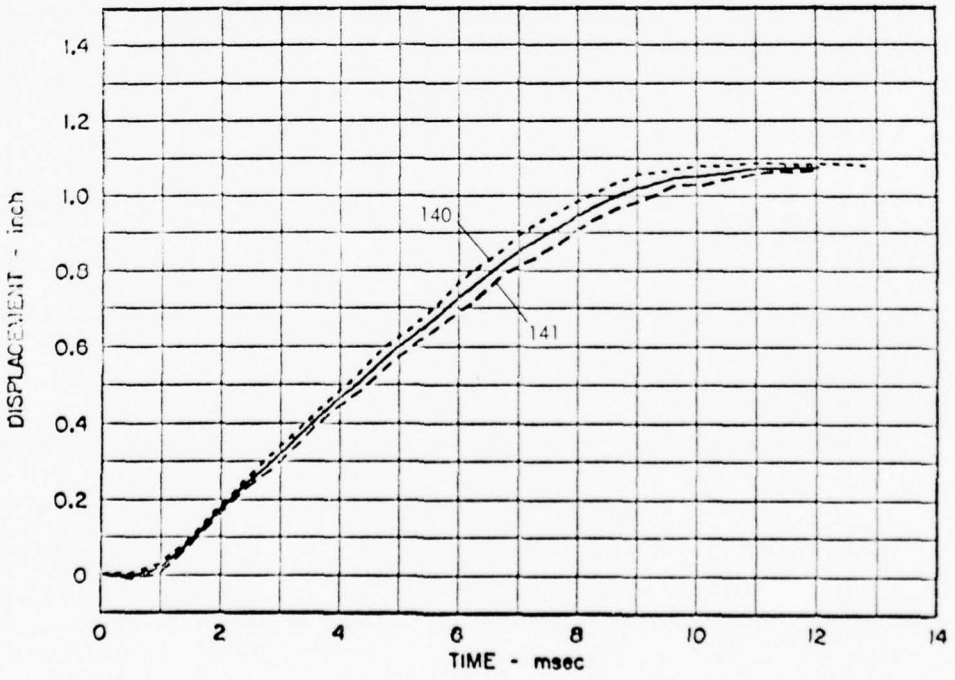

FIGURE 25 PISTON DISPLACEMENTS FROM GROUP 2 TESTS 140 AND 141

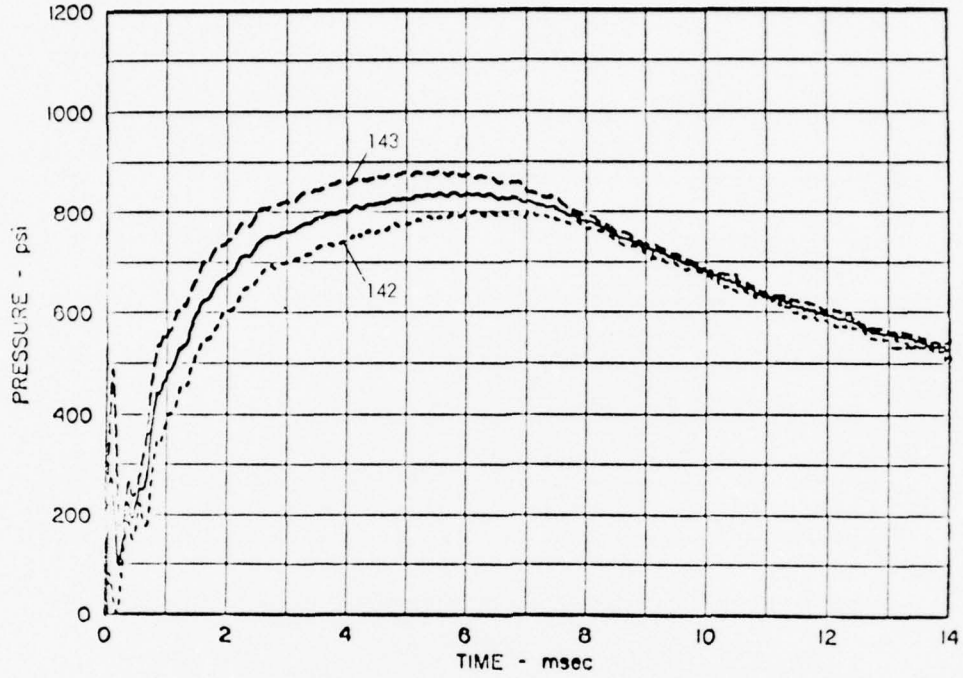

FIGURE 26 PRESSURE PULSES FROM GROUP 3 TESTS 142 AND 143

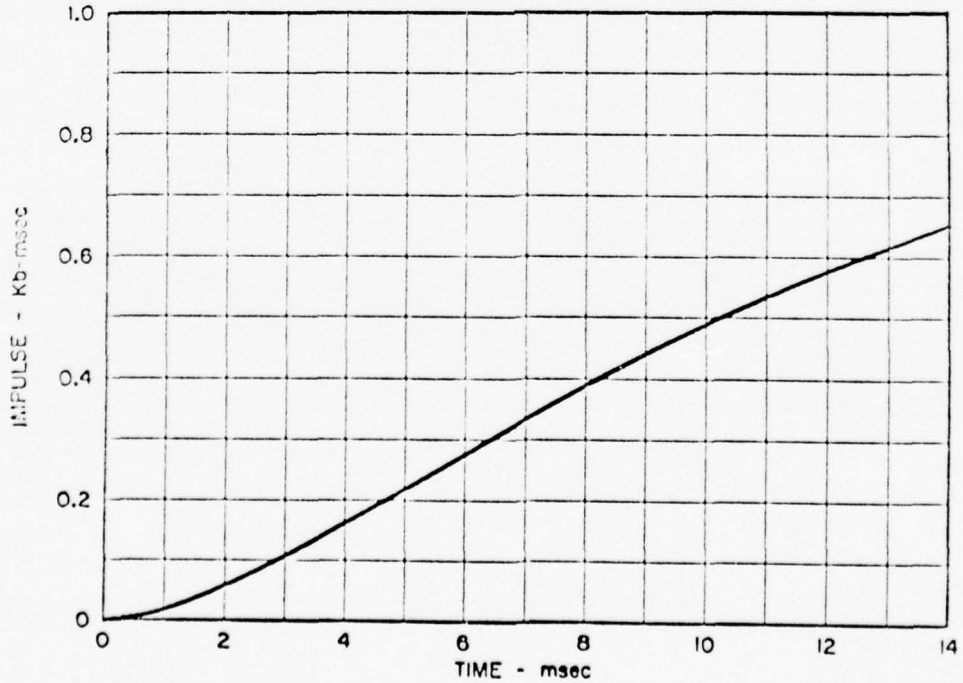

FIGURE 27 IMPULSES FROM GROUP 3 TESTS 142 AND 143

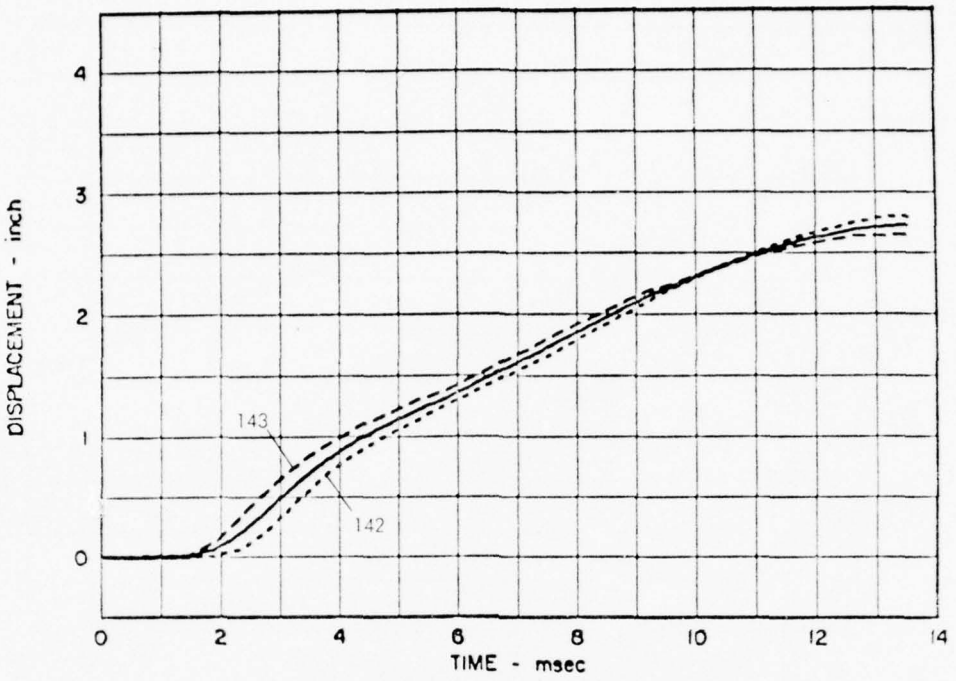

FIGURE 28 SLG FRONT DISPLACEMENTS FROM GROUP 3 TESTS 142 AND 143

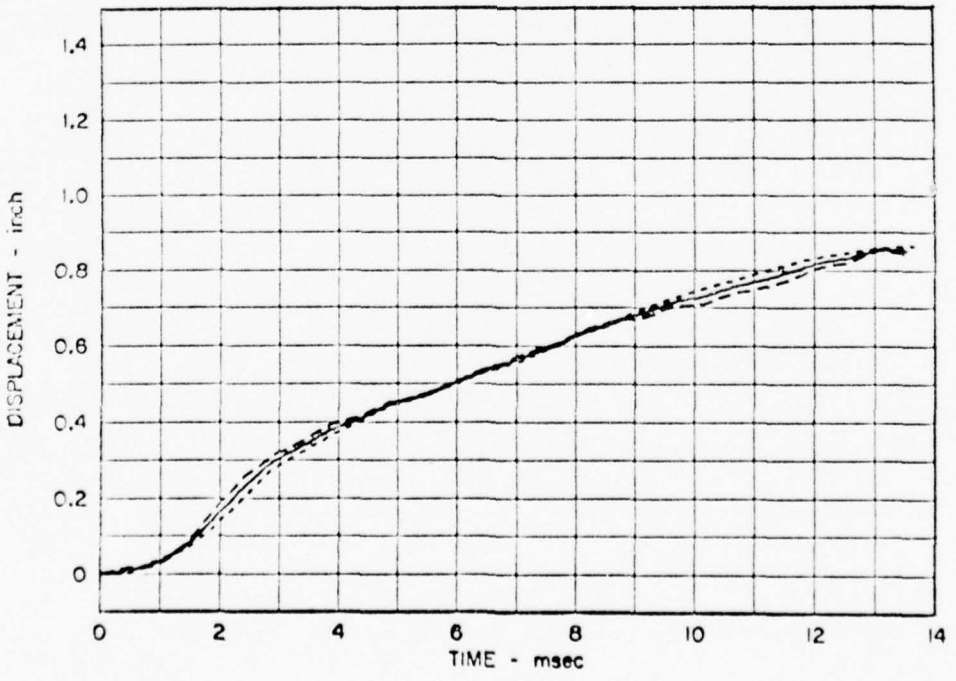

FIGURE 29 PISTON DISPLACEMENTS FROM GROUP 3 TESTS 142 AND 143

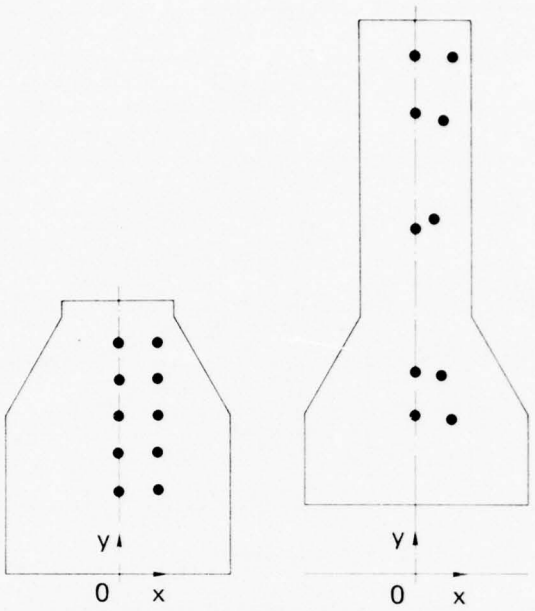

SHOT 134

MA-3702-141

FIGURE 30 INITIAL AND FINAL PARTICLE LOCATIONS FROM GROUP 1 TEST 134

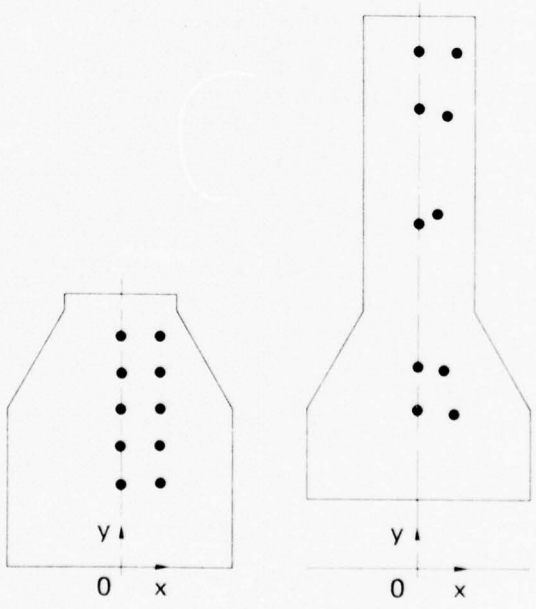

SHOT 135

MA-3701-142

FIGURE 31 INITIAL AND FINAL PARTICLE LOCATIONS FROM GROUP 1 TEST 135

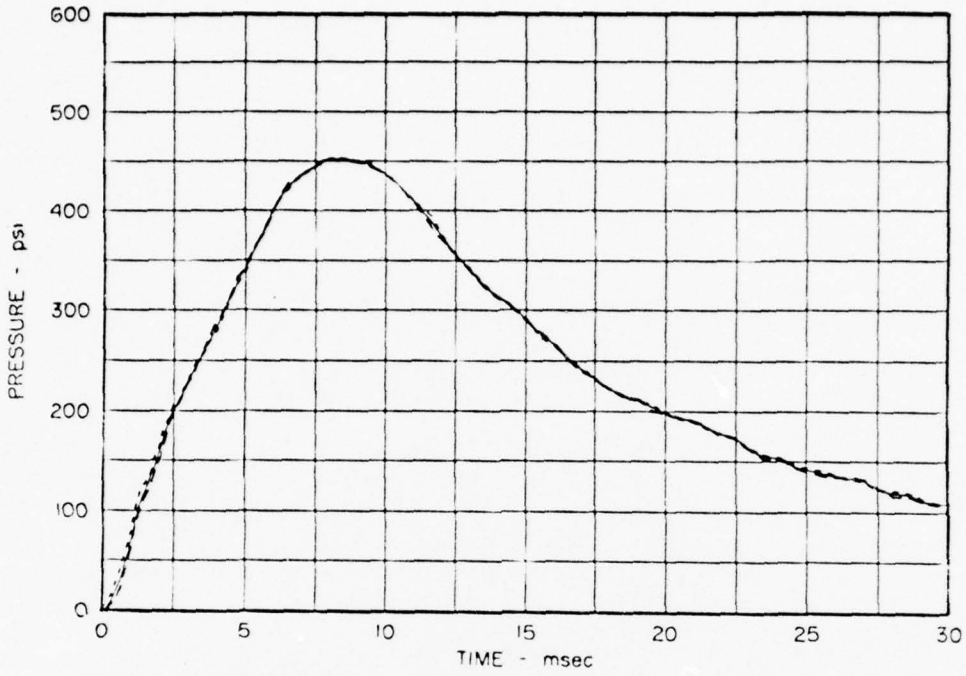

FIGURE 32 PRESSURE PULSES FROM FRICTION TEST 111

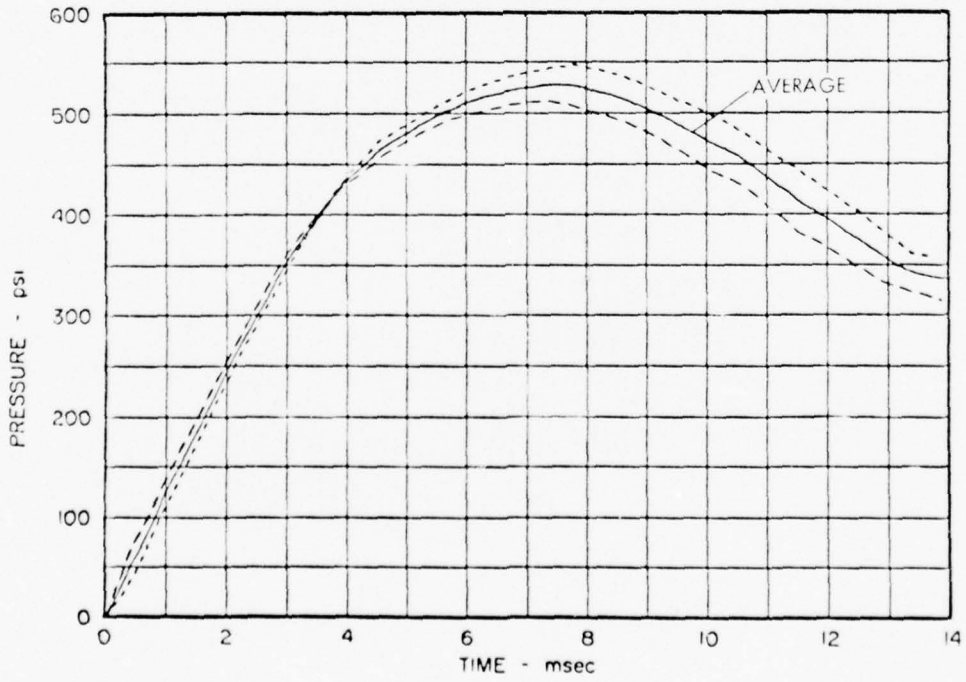

FIGURE 33 PRESSURE PULSES FROM FRICTION TEST 121

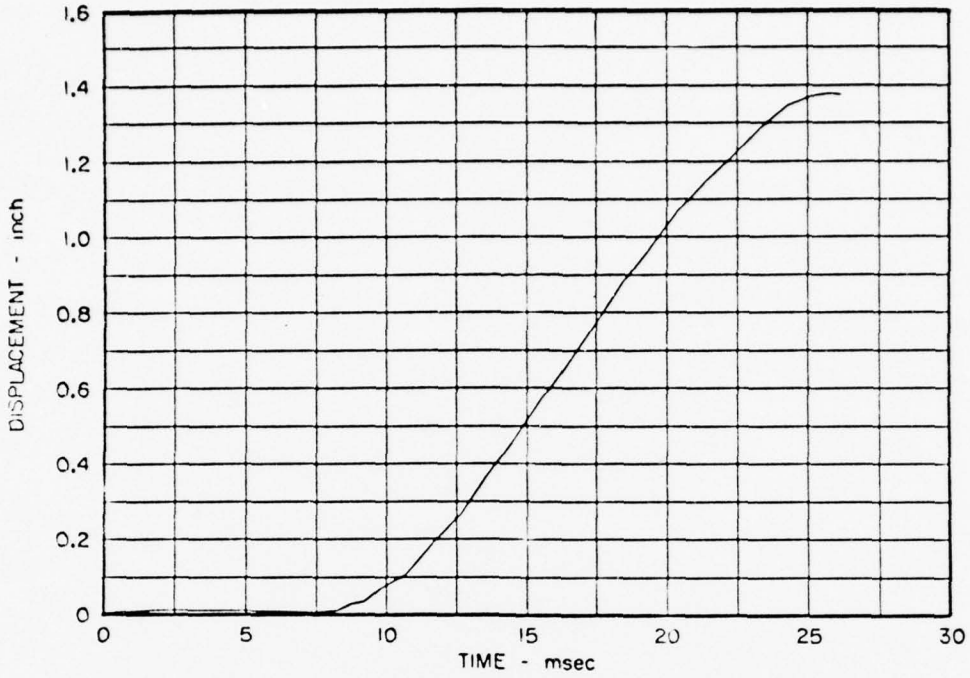

FIGURE 34 PISTON DISPLACEMENT FOR FRICTION TEST 111

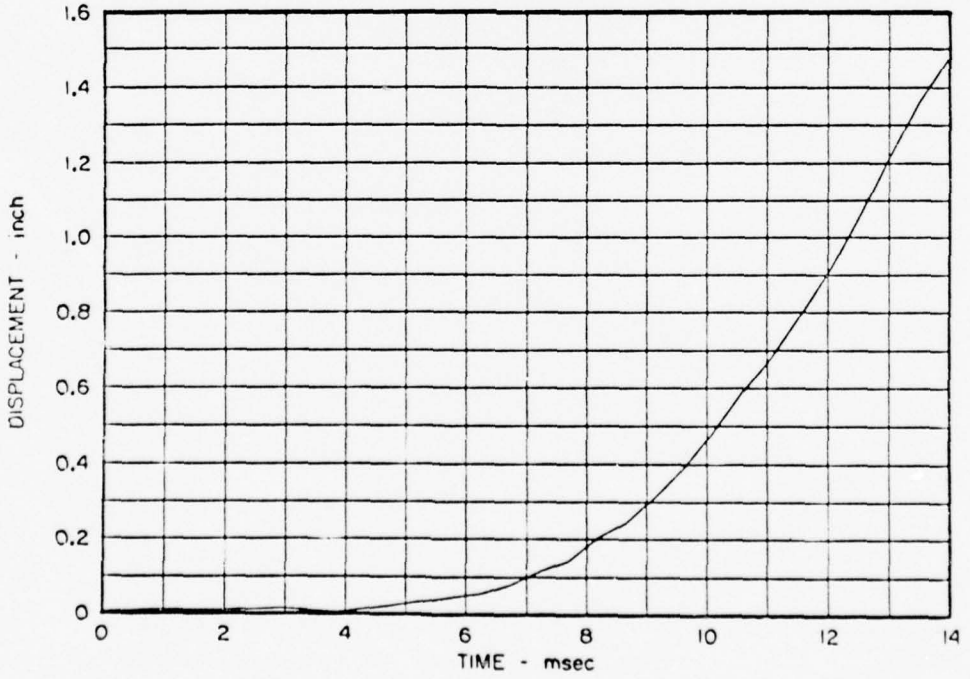

FIGURE 35 PISTON DISPLACEMENT FOR FRICTION TEST 121

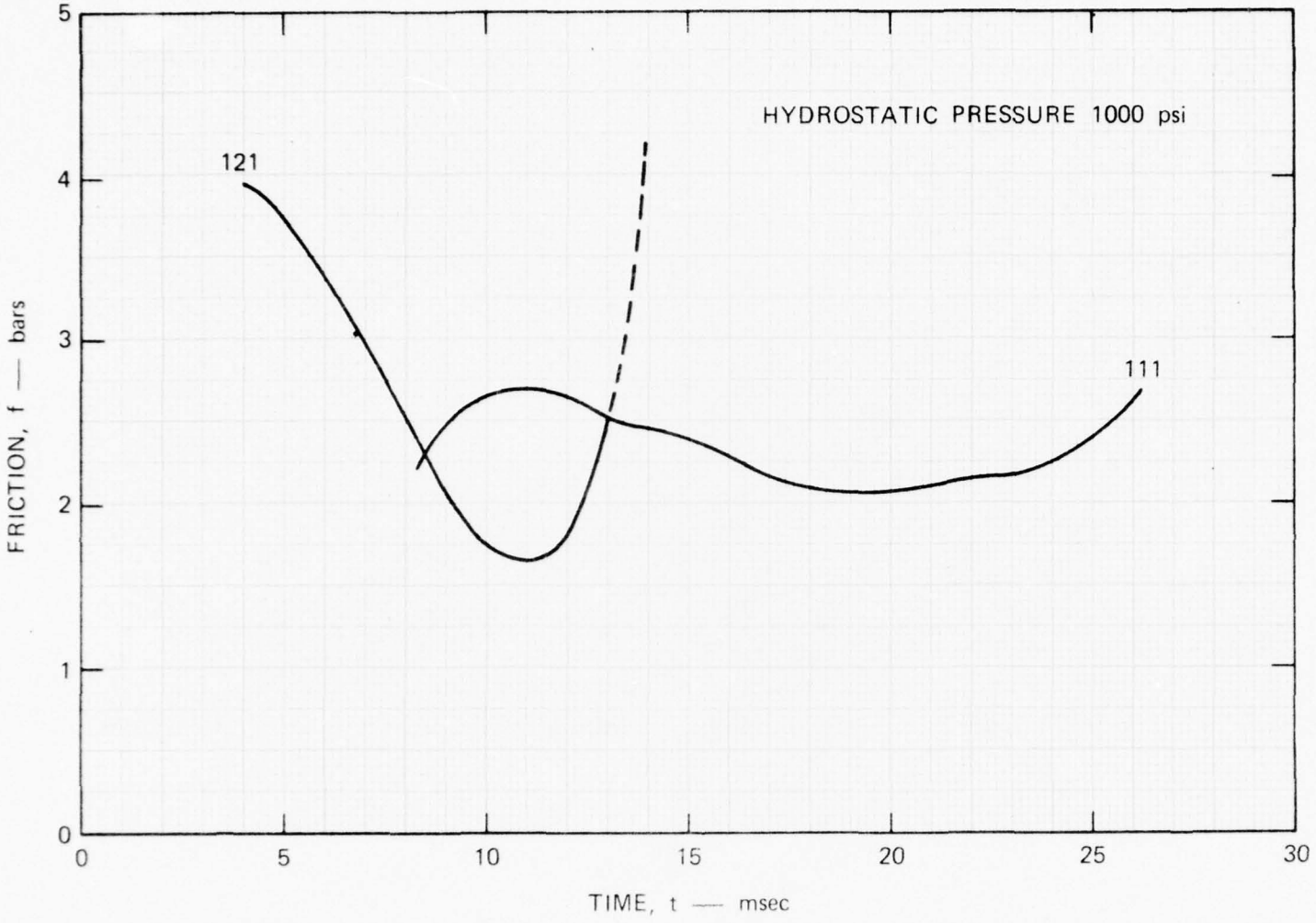

FIGURE 36 FRICTION RESULTS FROM TESTS 111 AND 121

Table 5

SLG PHYSICAL PROPERTIES

Test Sample	Densities (gm/cm^3)			Water % (Wet Weight)	Porosity %	Saturation %	Air Voids %	Unconfined Crush Strength psi
	Aged	Dry	Grain					
134 135	1.75	1.32	2.59	24	49	88	6	124
140 141 142 143	1.70	1.36	2.57	20	47	73	13	156
134[a]	1.74	1.30	2.59	25.3	50	88	6	
135[a]	1.74	1.30	2.59	24.7	49	88	6	
111	1.80	1.34	2.58	25	48	96	2	155
158 159	1.76	1.33	2.59	25	49	88	6	166 174

[a]Samples from extruded grout.

Table 6

MIXTURE FOR SUPERLEAN GROUT HSSL-1A

[a]Nevada Test Site Fines	72.5 %
Type G Portland Cement	3.2 %
Bentonite (Gel)	2.3 %
[b]CFR 2	0.03%
Water	22.0 %

[a]Material passing through No. 7 sieve (retains 2.5 mm dia particles).

[b]Concrete friction reducing compound 2 (detergent powder).

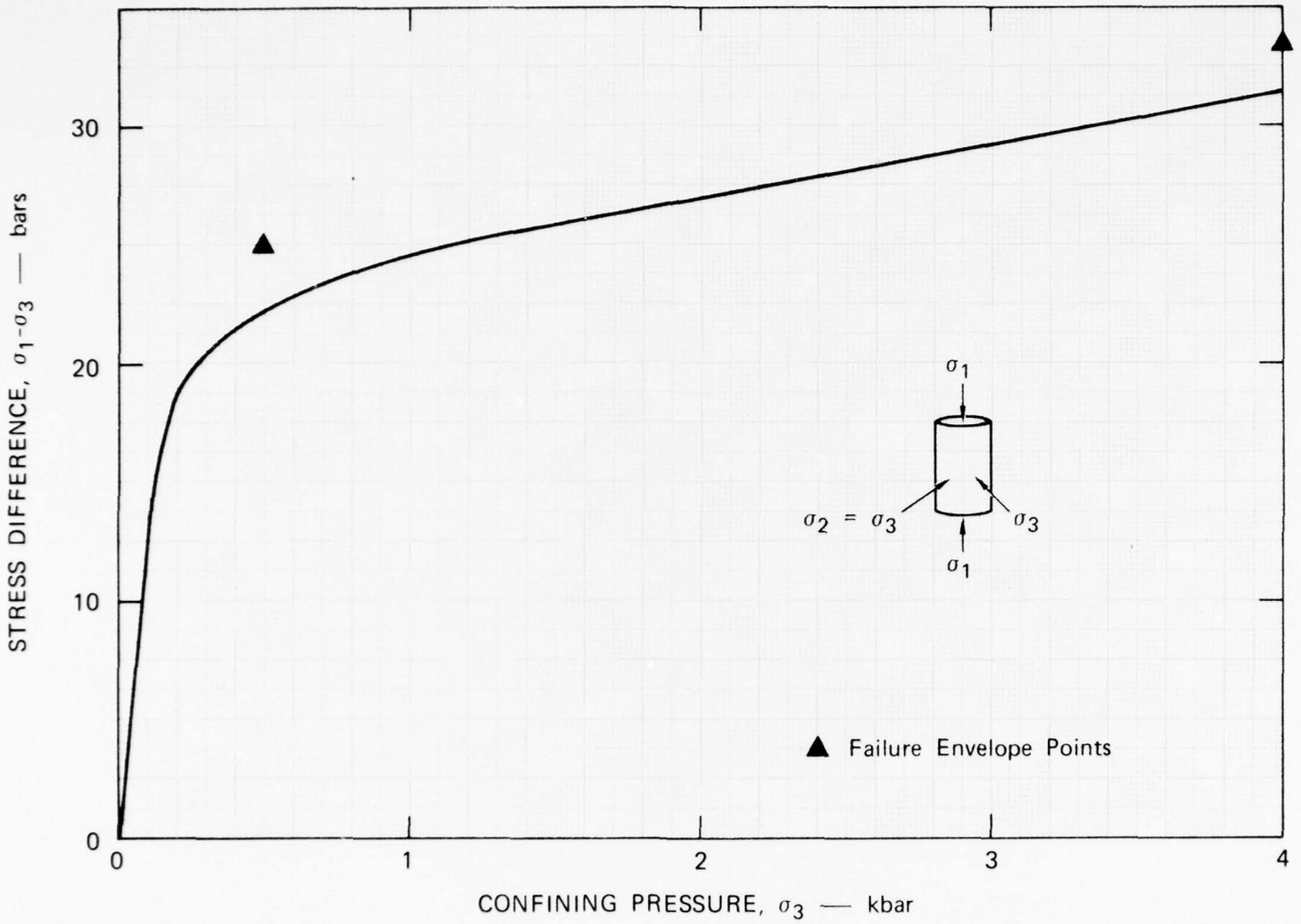

FIGURE 37 STRENGTH PROPERTIES OF SLG (UNIAXIAL STRAIN)

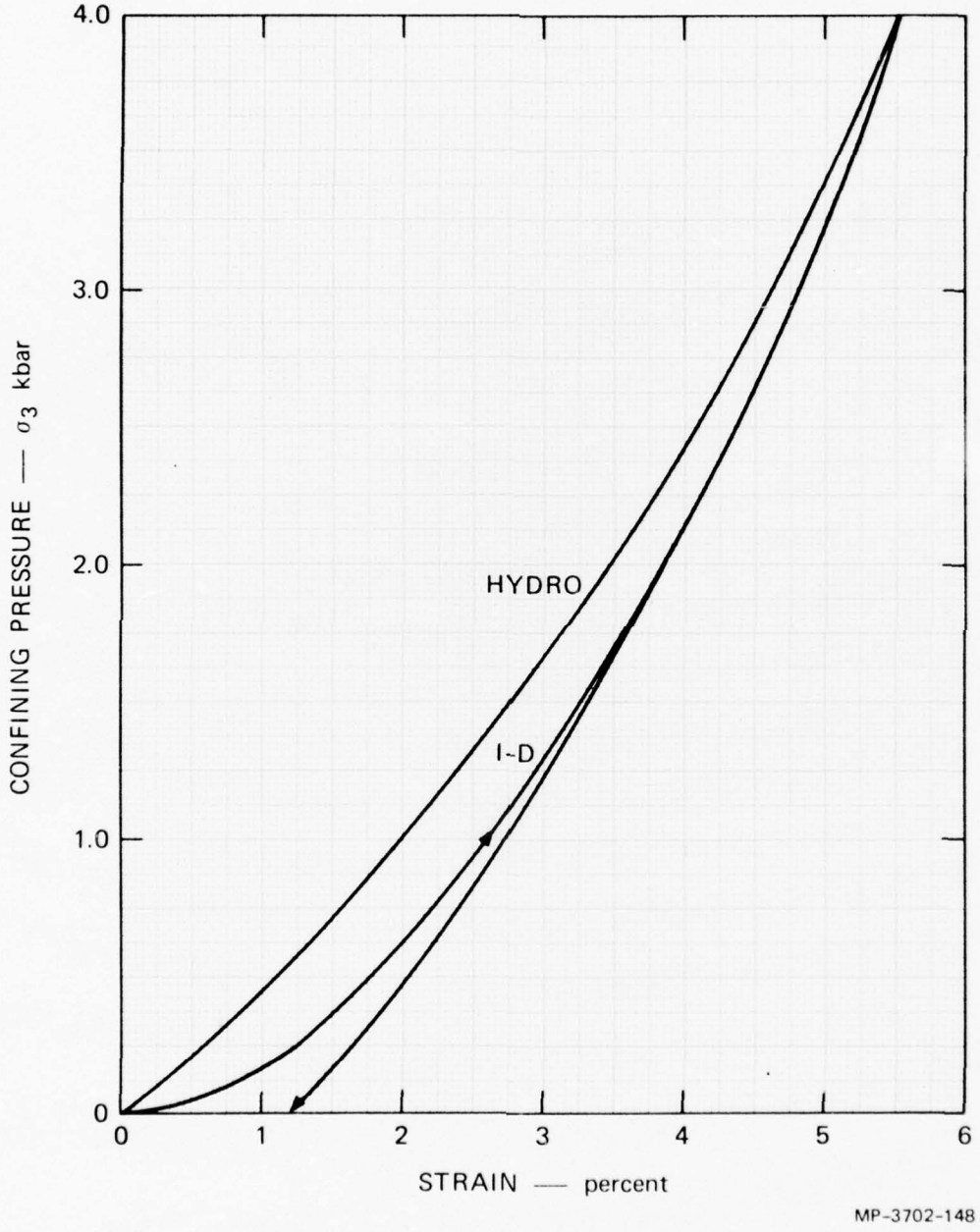

FIGURE 38 STRENGTH PROPERTIES OF SLG

Table 7

SIZE DISTRIBUTIONS OF NEVADA TEST SITE FINES FOR SIX SAMPLES

Particle Diameter (mm)	Percentage[a]					
	1	2	3	4	5	6
2.00	73.3	87.1	77.5	86.1	72.2	77.0
1.19	56.0	64.7	60.9	72.6	58.5	62.8
0.50	25.7	29.5	30.0	38.3	30.4	33.1
0.23	11.8	14.7	14.6	19.1	15.3	16.9
0.15	7.6	10.2	8.7	12.5	10.4	11.4

[a]Example: In Sample 3,
77.5 wt% of the total sample passed through a sieve that retains particles larger than 2 mm diameter,

60.9 wt% of the total sample passed through a sieve that retains particles larger than 1.19 mm diameter, and so on.

Table 8

DESIGN DISTRIBUTIONS OF NEVADA TEST SITE FINES

Particle Diameter (mm)	Percentage[a]		
	Average	Coarse	Very Coarse
2.0	80	72	70
1.19	60	55	45
0.50	30	26	20
0.23	16	11	10
0.15	10	8	5
	Unconfined Crush Strength (psi)		
	87	110	166
	107	134	185

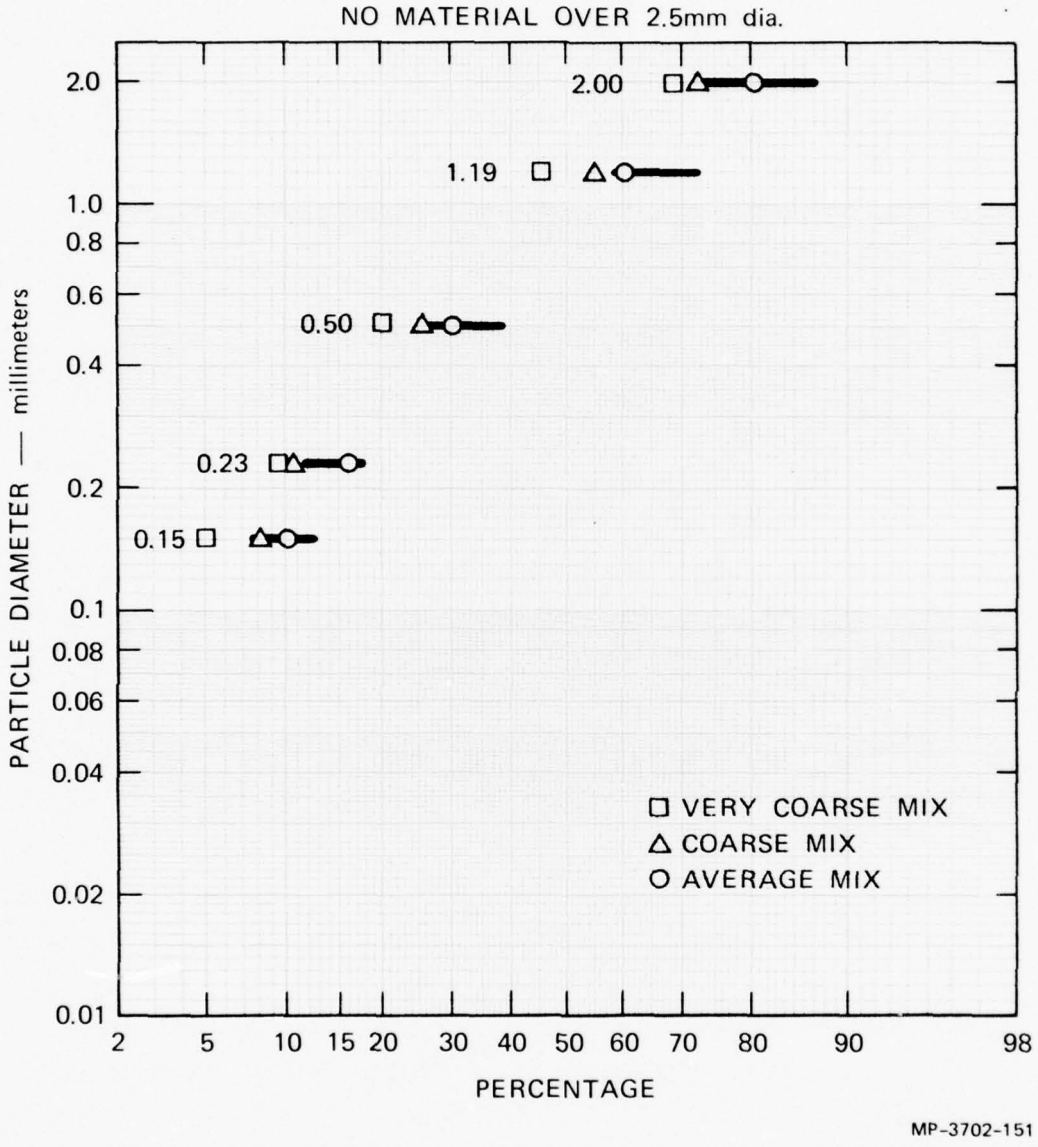

FIGURE 39 CUMULATIVE PARTICLE SIZE DISTRIBUTION FOR NEVADA TEST SITE FINES

IV CONTAINMENT EXPERIMENTAL RESULTS

Table 9 lists the principal constant flow rate hydrofracture tests conducted on 12-inch-diameter RMG spheres under 1000 psi overburden pressure with either exploded or unexploded cavities. The tests may be divided into three groups:

1. Tests 150 to 153 for obtaining the fracture pressure in an unexploded cavity.
2. Tests 154 and 155 for obtaining the fracture pressure in an exploded cavity.
3. Tests 160 to 163 for obtaining the local fracture pressure away from the cavity.

Comparison of results within each group, provides a measure of reproducibility. An overall quantitative measure of the effect of a residual stress field on the ability of the material to contain cavity gases is obtained by comparing the maximum cavity fracture pressures of the first and second groups. These values are 1670 and 2480 psi, respectively; thus, the residual stress field increases the fracture pressure by about 50% in these tests.

Unexploded Cavity Tests 150-153 were conducted in the configuration of Figure 40. The pressure-flow plots of Figure 41 were constructed from the complete hydrofracture records, to allow an assessment of reproducibility; plotting continued until flow was stopped. The fracture pressures are listed in Table 9 as 1680, 1645, 1640, and 1710 psi with an average of 1670 psi. The quantity of fluid pumped in at a flow rate of 4.26 cm^3/minute ranges from 7.8 to 9.4 cm^3 at fracture, the total system volume being about 91 cm^3 (Table 1). Compressibility of a fluid with a bulk modulus of 330,000 psi accounts for only 0.46 cm^3 of the total volume at 1700 psi.

Treating the RMG sphere as an elastic material of shear modulus $G = 10^6$ psi about to yield with an internal pressure of P_s = 1700 psi

and a pressure at infinity of P_∞ = 1000 psi, gives an estimate of only 0.016 cm^3 for the increase in cavity volume before fracture. The piping system with gages can absorb about 2.5 cm^3 at 1700 psi. Thus, most of the fluid is being forced either into the rock pores from the cavity wall or around the access pipe.

As shown in Figure 41, the cavity pressure drops rapidly following fracture, because fluid can now flow into the thin plane of the crack. The minimum pressure ranges from 1100 to 1300 psi. A gradual rise in pressure follows, implying resistance to hydrofracture; after 25 cm^3 of flow, the pressures range from 1150 to 1450 psi.

The sphere was removed from the pressure vessel after release of the internal pressure followed by release of the overburden pressure. In each case, a crack was visible around almost the entire circumference. The two halves were tapped apart by use of a broad chisel. Figure 49 shows the exposed fracture plane and the extent of the dyed Glycerin fluid in Test 150. Fracture occurred out of the plane of the access pipe; thus, the pipe probably does not introduce a stress concentration for crack initiation. For comparison with the fracture behavior in the presence of a residual stress field note that the flow is from the cavity outward and surrounds the cavity in a fairly uniform manner.

The configuration of Figure 42 was used in Exploded Cavity Tests 154 and 155. The pressure-flow plots of Figure 43 were constructed from the complete hydrofracture records to allow an assessment of reproducibility; plotting continued until flow was stopped. Fracture occurs at 2500 and 2060 psi and the maximum pressures achieved are 2460 and 2620 psi. The quantities of fluid pumped in at a flow rate of 4.26 cm^3/minute are 3.5 and 6 cm^3. These values are below the range of 7.8 to 9.4 cm^3 for the Unexploded Cavity Tests 150 and 153, implying that the material around the exploded cavity is less permeable because of crushing of the pores.

In both tests, the pressure drops by about 100 psi after fracture, considerably less than in Tests 150 to 153. This pressure drop implies that the extent of initial fracture is reduced by the compressive residual

stress field. The pressure now rises steeply to exceed the initial fracture pressure, probably because of the compressive stress field resistance to crack propagation. In Test 154, it appears as if a second fracture is initiated at a pressure of 2450 psi and a fluid flow of 7 cm^3. The pressure then drops by 150 psi and gradually increases to 2460 psi at about 15.7 cm^3 before suddenly dropping to 1400 psi. In Test 155, an apparent second fracture does not occur. The pressure rises to its maximum at 2620 psi and drops suddenly to 1300 psi at about 10.5 cm^3. The sudden pressure drops are attributed to the cracking breaking through highly compressive residual stress field.

The sphere was removed from the pressure vessel after release of the internal pressure followed by release of the overburden pressure. In each case, a crack was visible around almost the entire circumference. The two halves were tapped apart by use of a broad chisel. Figure 50 shows the exposed fracture plane and the extent of the dyed Glycerin fluid in Test 155. The dyed fracture area surrounds the cavity circle but lies outside an irregular annular region of unfractured material that coincides with the region of compressive residual stress. The exposed fracture plane is intersected by another orthogonal fracture plane. This second plane is dyed and intersects the cavity.

The photographs of Figure 48 show the corresponding results for Test 146, an earlier test performed at a slower flow rate (0.71 cm^3/minute). The dyed region is less extensive but the character is the same, a breaking through of the high residual stress field region adjacent to the cavity followed by spreading hydrofracture in the low residual stress field region beyond.

The configuration of Figure 44 was used in Exploded Cavity Tests 160 and 161. The pressure-flow plots of Figure 45 were constructed from the complete hydrofracture records to allow comparison. As shown in Figure 44, local pressurization of the grout away from the cavity is effected through four 1/8-inch-diameter holes in the access tube. The pressurization location is outside the region of predicted maximum residual stresses. Figure 45 shows that the pressure histories are highly

oscillatory in these two tests and that the general pressure levels are different. This behavior probably stems from the highly localized complicated configuration where the grout is pressurized, providing many stress concentration zones for local crack initiation. Figure 51 shows the main fracture plane for Test 161. The dyed region indicates that the crack was forced to spread around the central spherically annular region of high compressive residual stress. A feature not previously observed appears in Figure 51: a crack that is approximately spherical, almost surrounding the cavity but located eccentrically; this feature was not observed in Test 160. Formation of such a circumferential crack is consistent with the residual stress field in this region where the radial stress component is predicted to be less compressive than the tangential stress component.

The configuration of Figure 46 was used in Exploded Cavity Tests 162 and 163. The pressure-flow plots of Figure 47 were constructed from the complete hydrofracture records to allow comparison. The configuration for local pressurization of the grout away from the cavity provides an exposed cylindrical grout surface 1/4 inch in diameter and 1 inch long; the objective was to simplify the configuration of Figure 44 for Tests 160 and 161. Figure 47 shows that the pressure histories are oscillatory with differing pressure levels, but the results show a marked improvement over those of Figure 45, with less oscillation and smaller pressure difference (2000 and 2300 psi). Figure 52 shows the main fracture plane for Test 163. The plane is almost tangential to the cavity. The dyed region indicates that the crack was forced to spread around the central, spherically annular region of high compressive residual stress.

Figure 53, like Figure 41, shows the pressure-flow curves for the unexploded cavity Tests 150 to 153 augmented by the curve for Test 147, because the only parameter difference is the smaller cavity size (0.65 in diameter compared with 1.13 in diameter for Test 147). The fracture pressure of 1470 psi in Test 147 is lower but comparable with the average pressure of 1670 psi for Tests 150 to 153. Fracture occurred after about 5 cm^3 of flow, which is well below the 7.8 to 9.4 cm^3 range for Tests 150 to 153. This lower flow value is attributable to the smaller spherical surface area available for fluid flow into the grout pores.

Figure 54, like Figure 43, shows the pressure-flow curves for the exploded cavity Tests 154 and 155 augmented by the curve for Test 146, because the only parameter difference is the smaller flow rate (0.71 cm^3/minute compared with 4.26 cm^3/minute) for Test 146. The fracture pressure for Test 146 is similar to that for Test 155 (2540 and 2500 psi), and the overall pressure history is similar. The interesting difference is the greater fluid flow that occurs before fracture in Test 146, specifically, 24 cm^3 compared with about 4 and 6 cm^3 in Tests 154 and 155. The greater flow is caused by the slower imposed flow rate allowing a greater volume of flow into the grout pores.

Table 9

SUMMARY LIST OF CONSTANT FLOW RATE TESTS[a]

Test	Cavity Dia Before (in.)	Cavity Dia After (in.)	Explosive Weight (gm)	Maximum Pressure (psi)	Configuration Type[b]	Figure	
146	0.65	1.16	1	2540	A	10,16	Exploded cavity pressurization (slow rate: 0.71 cm^3/min)[c]
150	1.13	1.13	-	1680	A	8,9,17,A-3	Unexploded cavity pressurization
151	1.14	1.14	-	1645	A	8,9,A-4	Repeat of 150
152	1.10	1.10	-	1640	A	8,9,A-5	Repeat of 150
153	1.15	1.15	-	1710	A	8,9,A-6	Repeat of 150
154	0.65	1.12	1	2460	A	10,11,A-7	Exploded cavity pressurization
155	0.65	1.10	1	2500	A	10,11,18, A-8	Repeat of 154
160	0.65	1.15	1	2070	B	12,13,A-9	Far-field local pressurization (no cavity pressure)
161	0.65	1.15	1	3260	B	12,13,A-10	Repeat of 160
162	0.65	1.08	1	1970	B	14,15,A-11	Far-field local pressurization (no cavity pressure)
163	0.65		1	2320	B	14,15,A-12	Repeat of 162

[a]Overburden pressure 1000 psi.

[b]Type A for pressurization in cavity; Type B for local pressurization away from cavity.

[c]Flow rate in remaining tests, 4.26 cm^3/min.

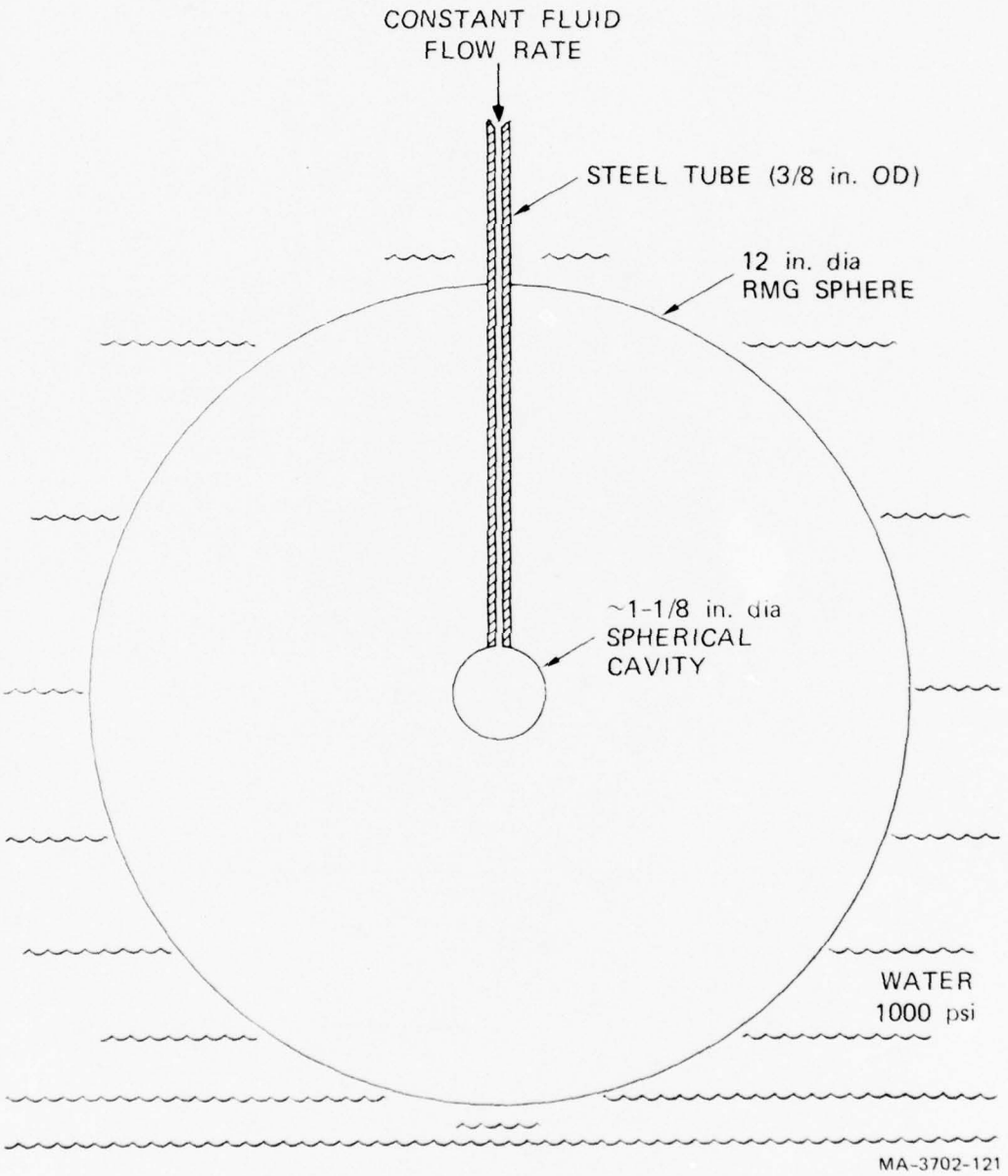

FIGURE 40 CONFIGURATION FOR UNEXPLODED CAVITY TESTS 150-153

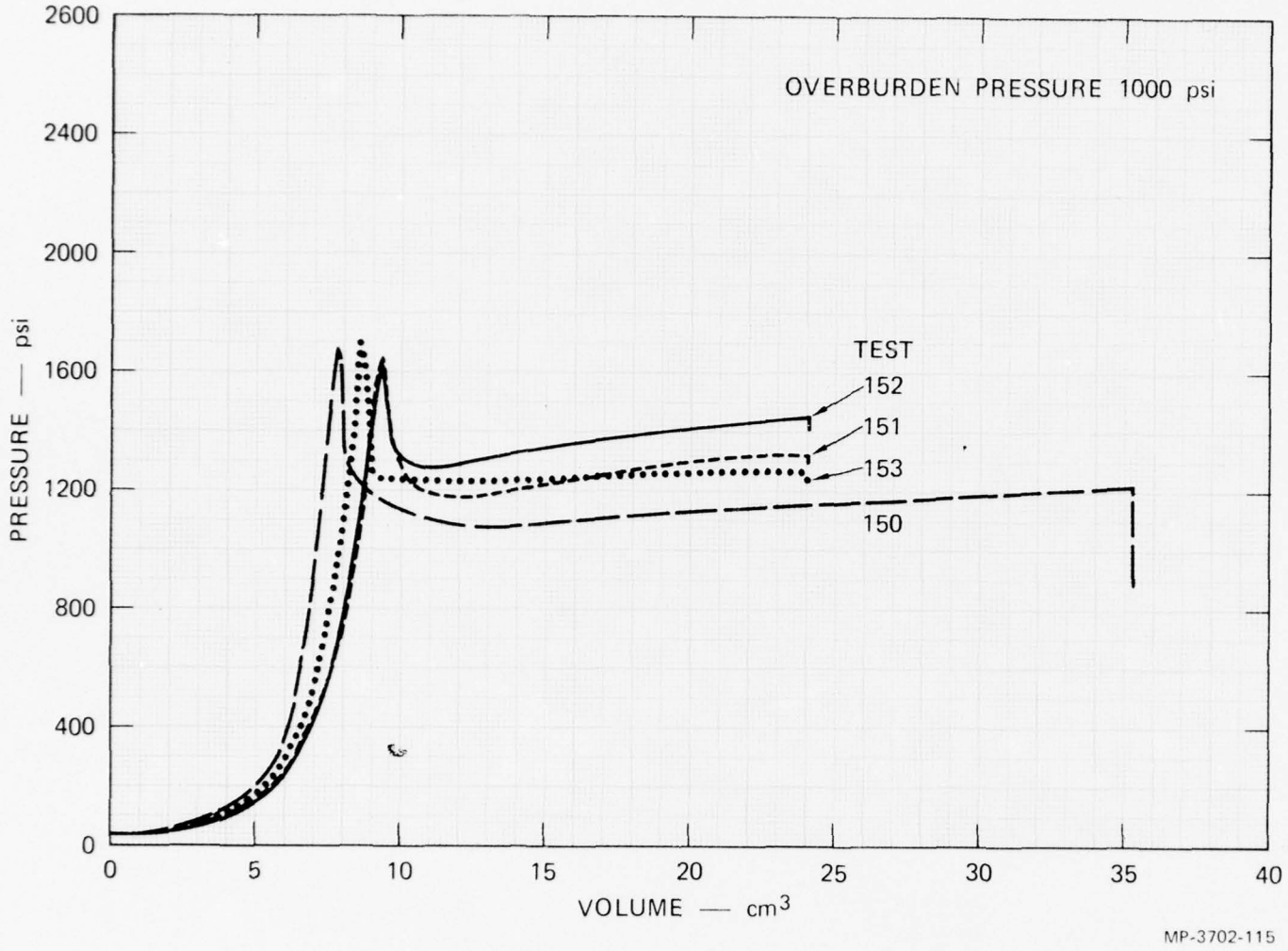

FIGURE 41 HYDROFRACTURE PRESSURES FOR UNEXPLODED CAVITY TESTS 150-153

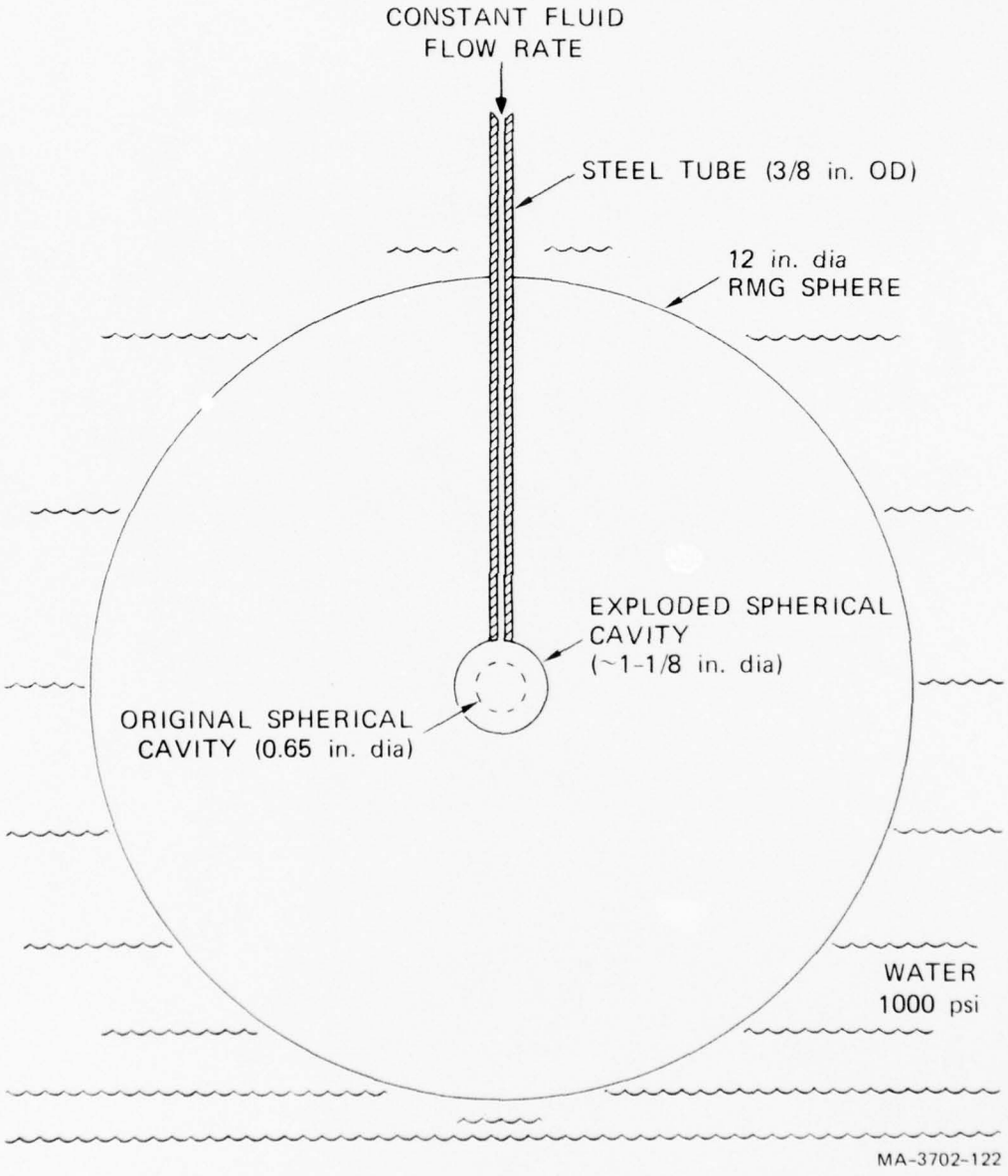

FIGURE 42 CONFIGURATION FOR EXPLODED CAVITY TESTS 154 AND 155

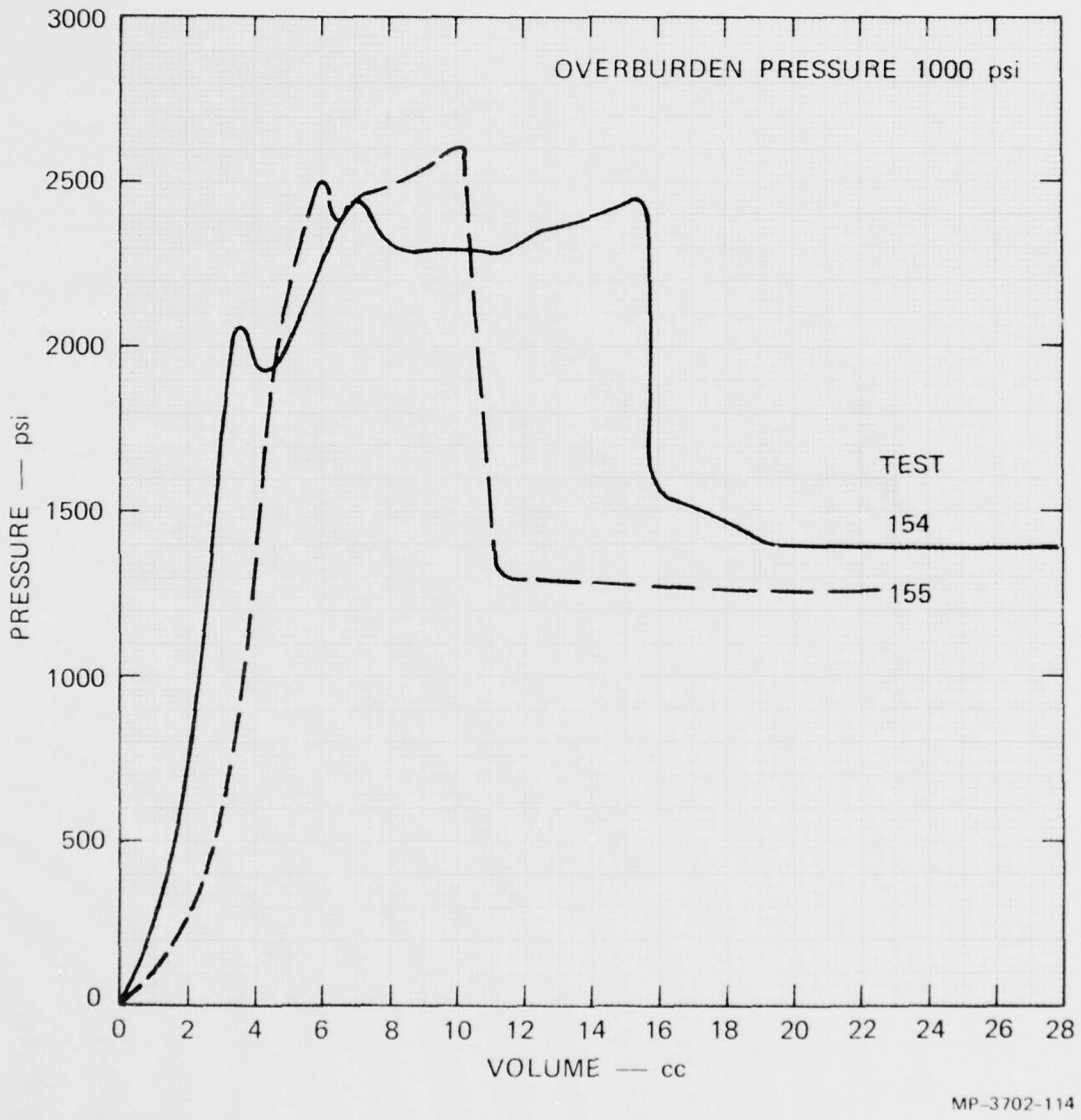

FIGURE 43 HYDROFRACTURE PRESSURES FOR EXPLODED CAVITY TESTS 154 AND 155

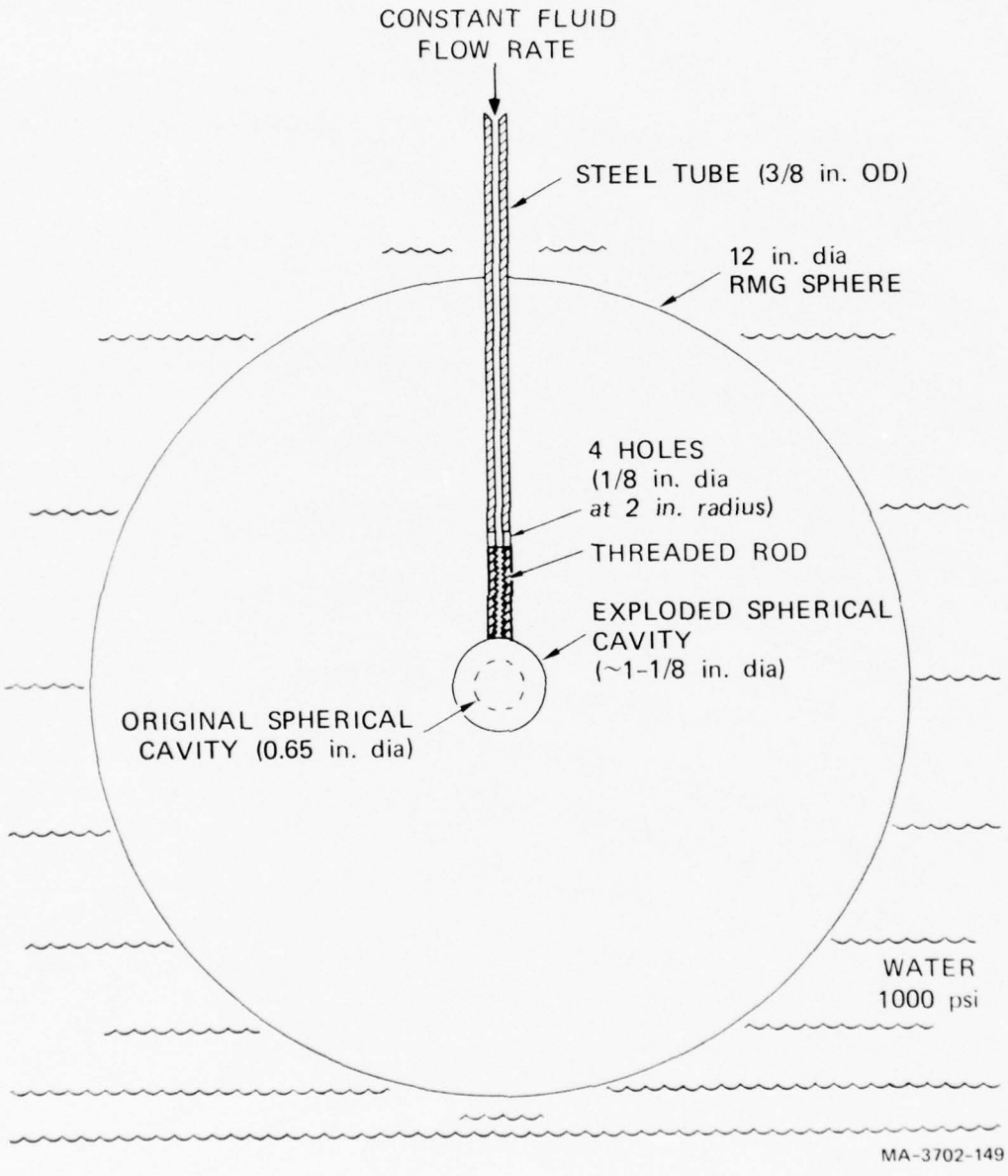

FIGURE 44 CONFIGURATION FOR EXPLODED CAVITY TESTS 160 AND 161

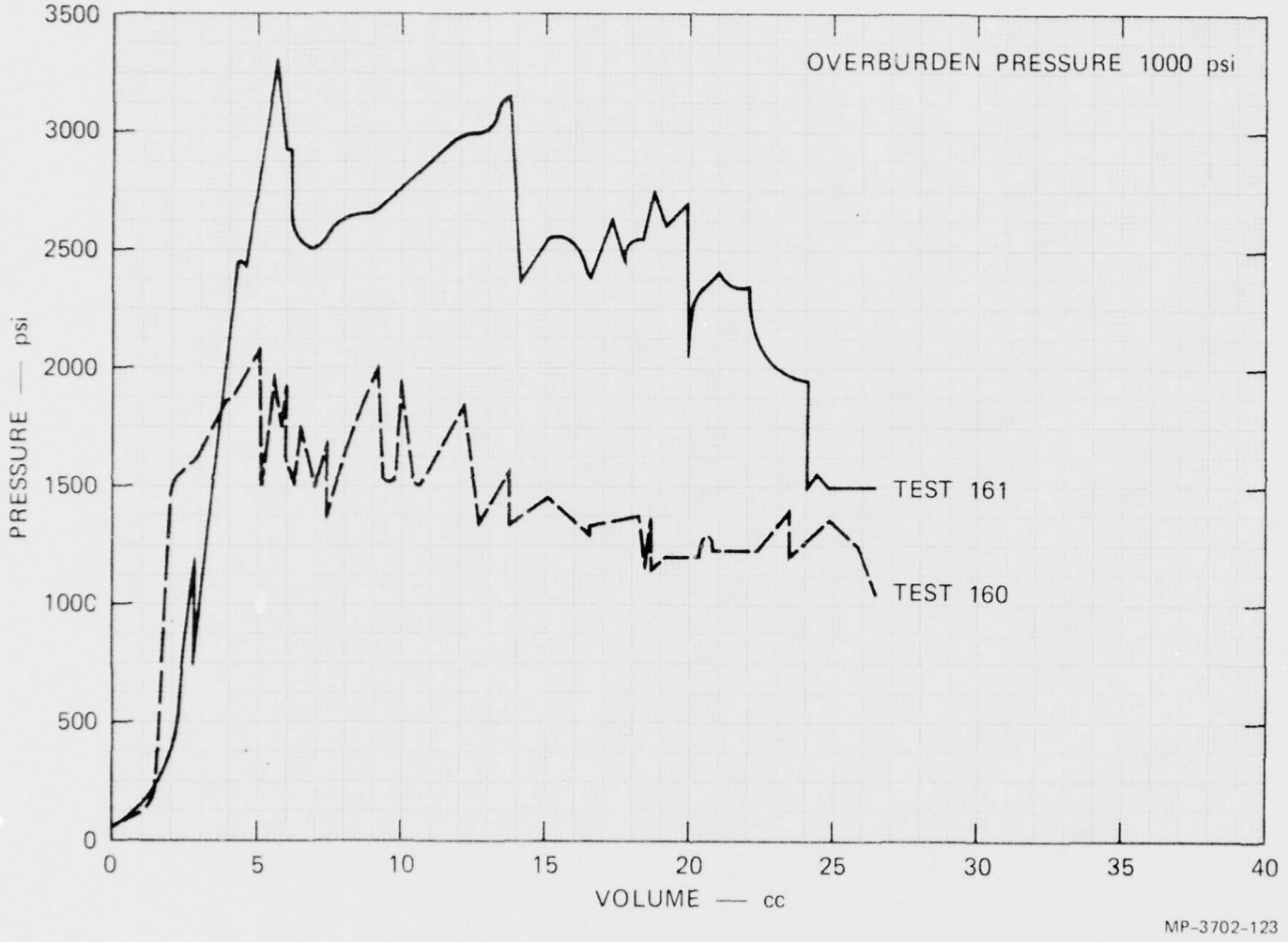

FIGURE 45 HYDROFRACTURE PRESSURES FOR EXPLODED CAVITY TESTS 160 AND 161

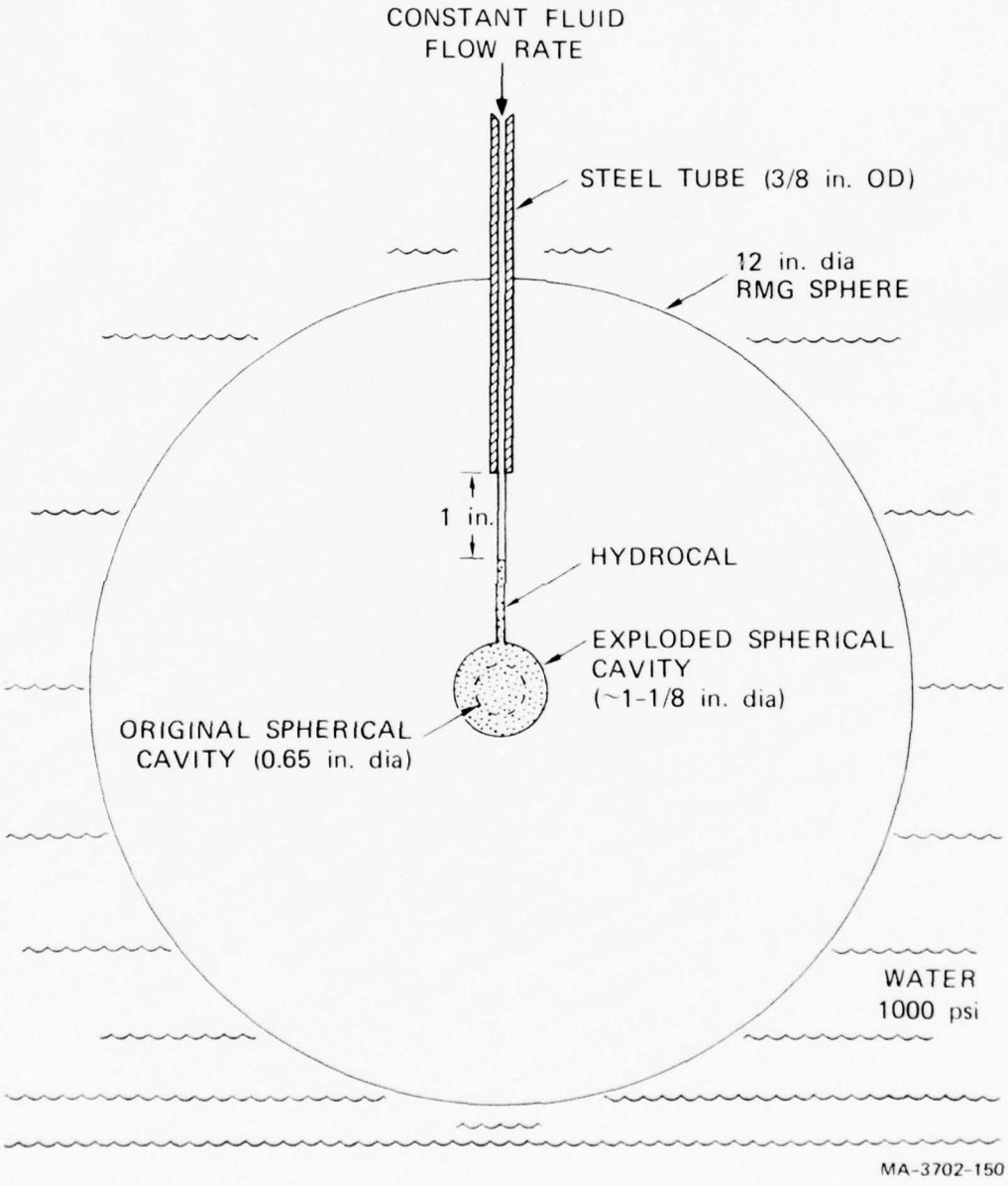

FIGURE 46 CONFIGURATION FOR EXPLODED CAVITY TESTS 162 AND 163

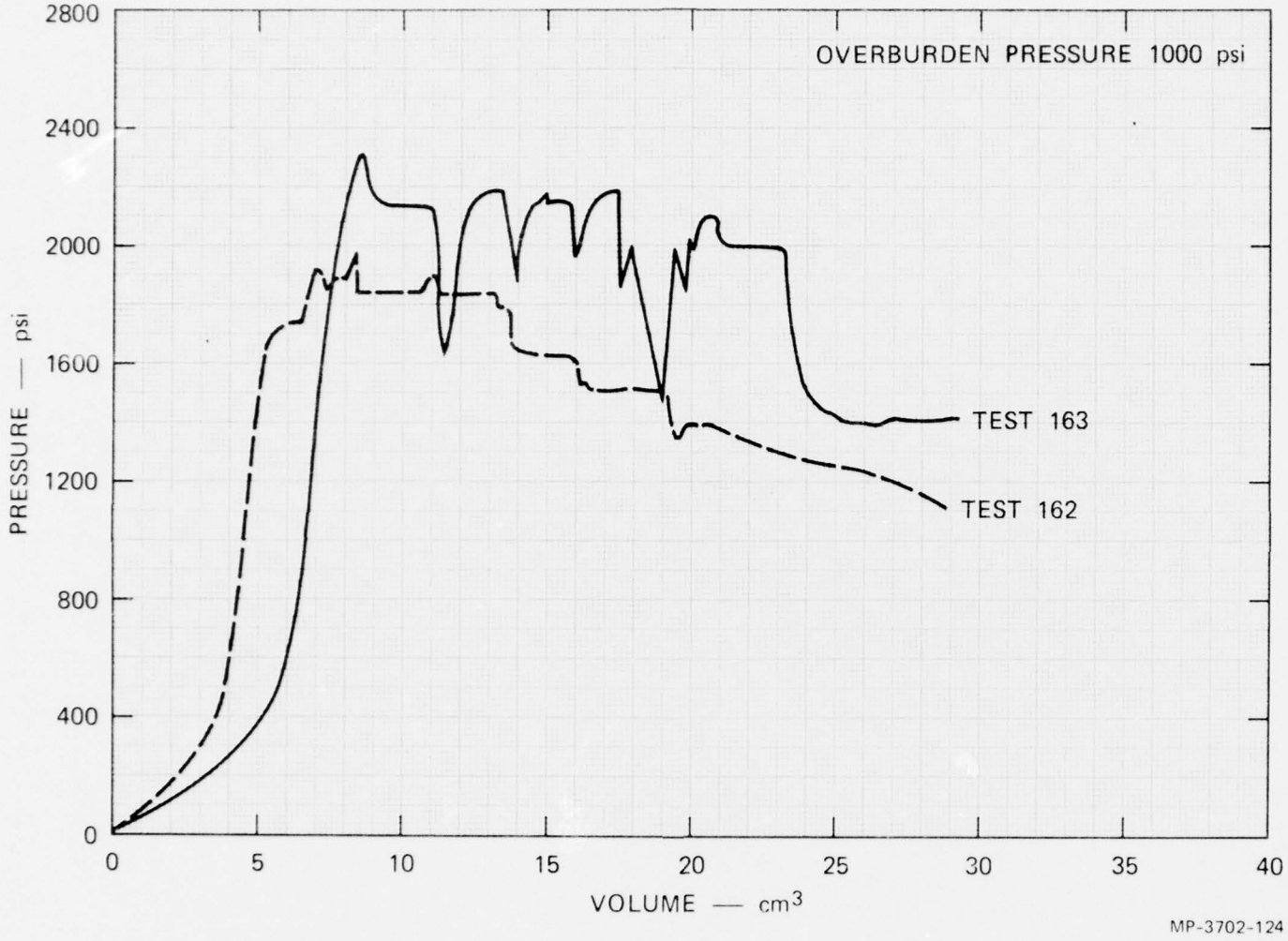

FIGURE 47 HYDROFRACTURE PRESSURES FOR EXPLODED CAVITY TESTS 162 AND 163

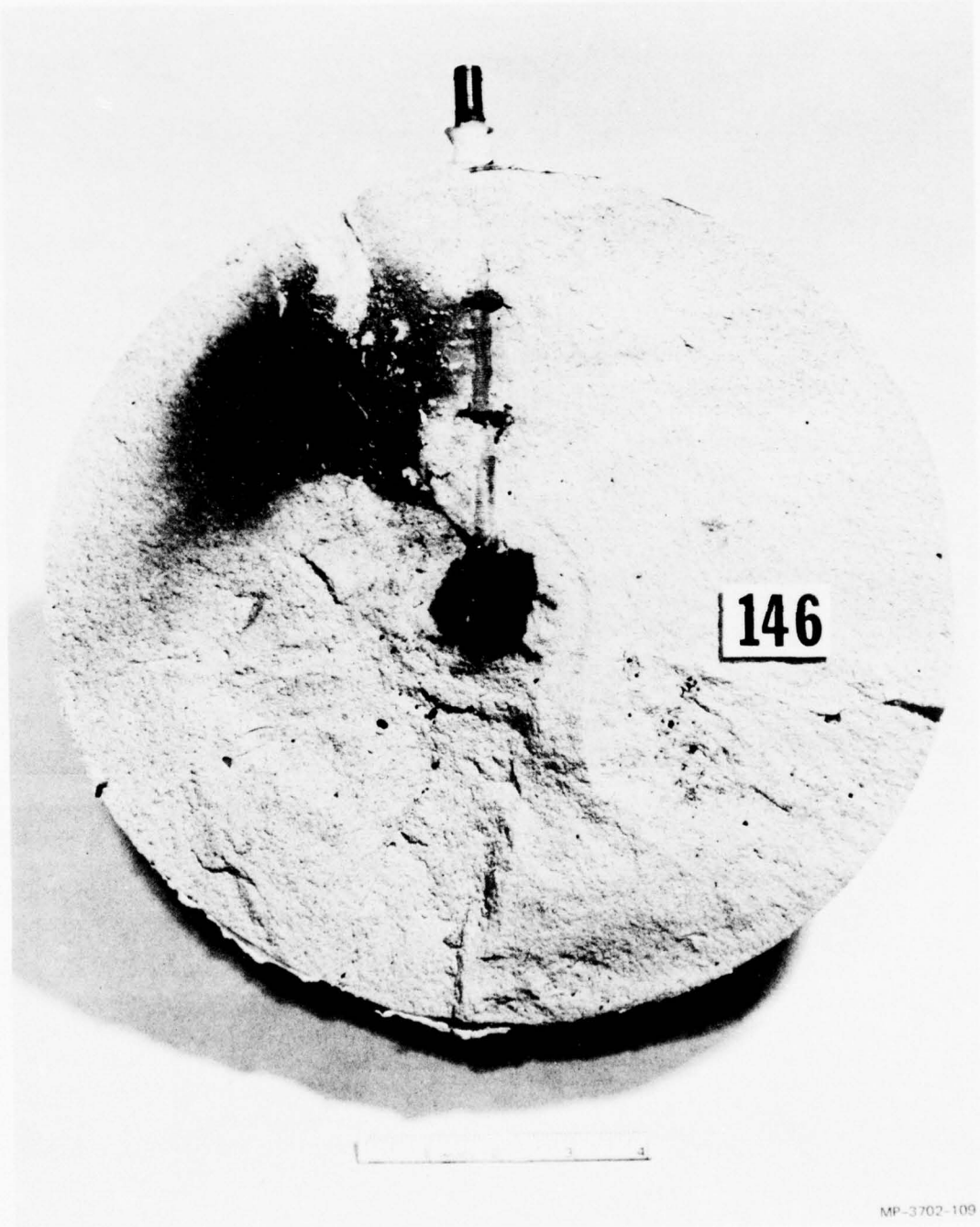

FIGURE 48 HYDROFRACTURE FROM AN EXPLODED CAVITY – TEST 146

FIGURE 48 HYDROFRACTURE FROM AN EXPLODED CAVITY – TEST 146 (Concluded)

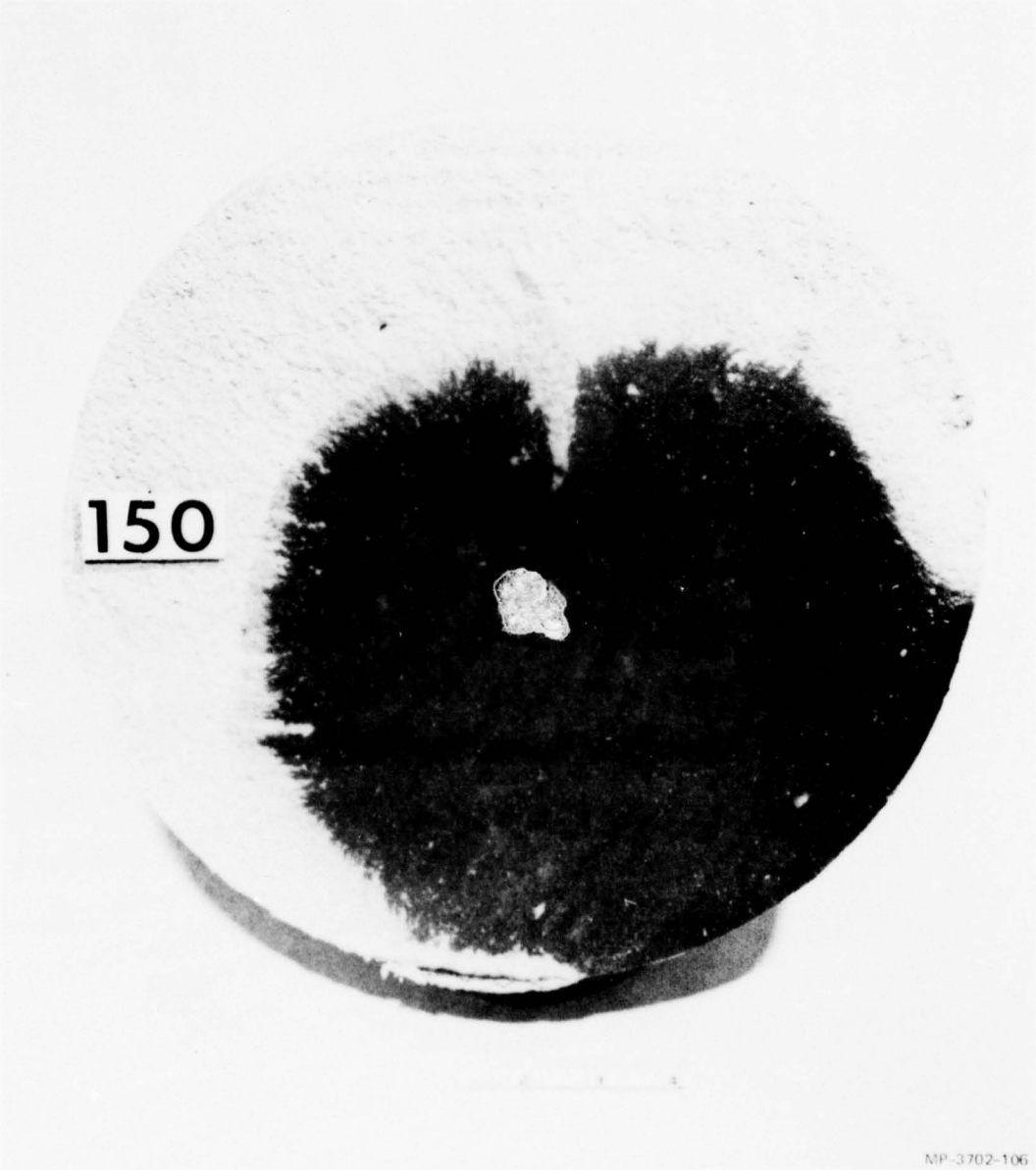

FIGURE 49 HYDROFRACTURE FROM AN UNEXPLODED CAVITY – TEST 150

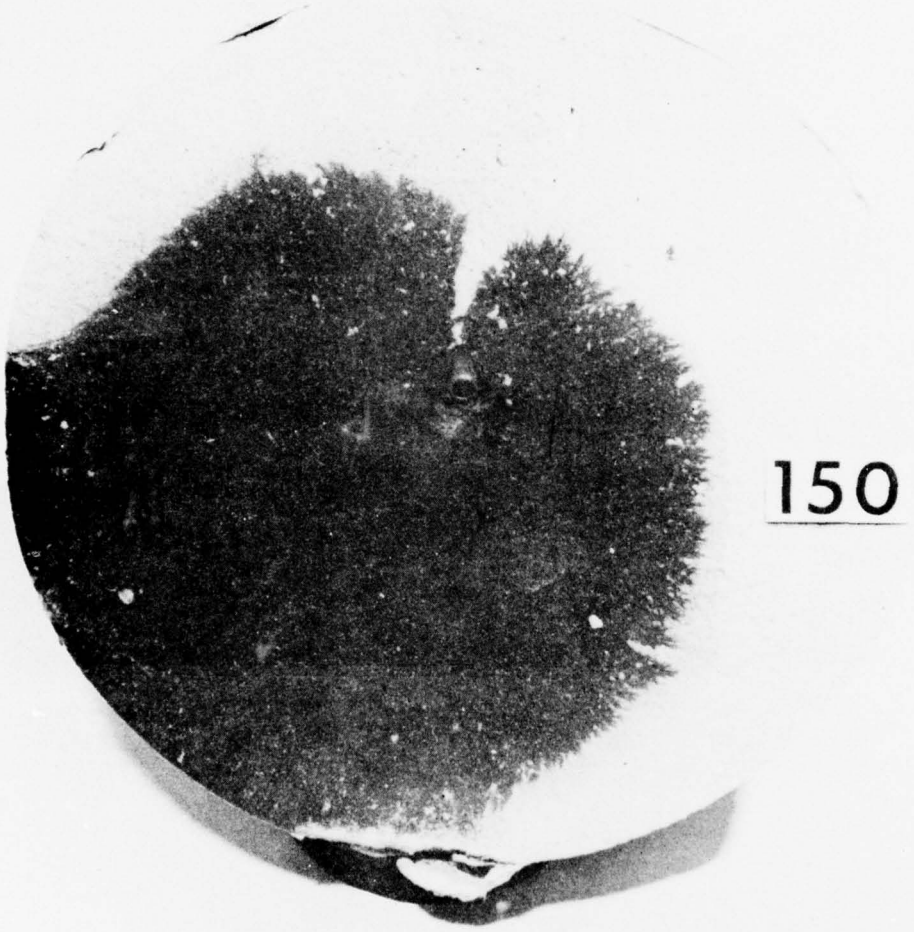

MP-3702-111

FIGURE 49 HYDROFRACTURE FROM AN UNEXPLODED CAVITY – TEST 150 (Concluded)

FIGURE 50 HYDROFRACTURE FROM AN EXPLODED CAVITY – TEST 155

FIGURE 50 HYDROFRACTURE FROM AN EXPLODED CAVITY – TEST 155 (Concluded)

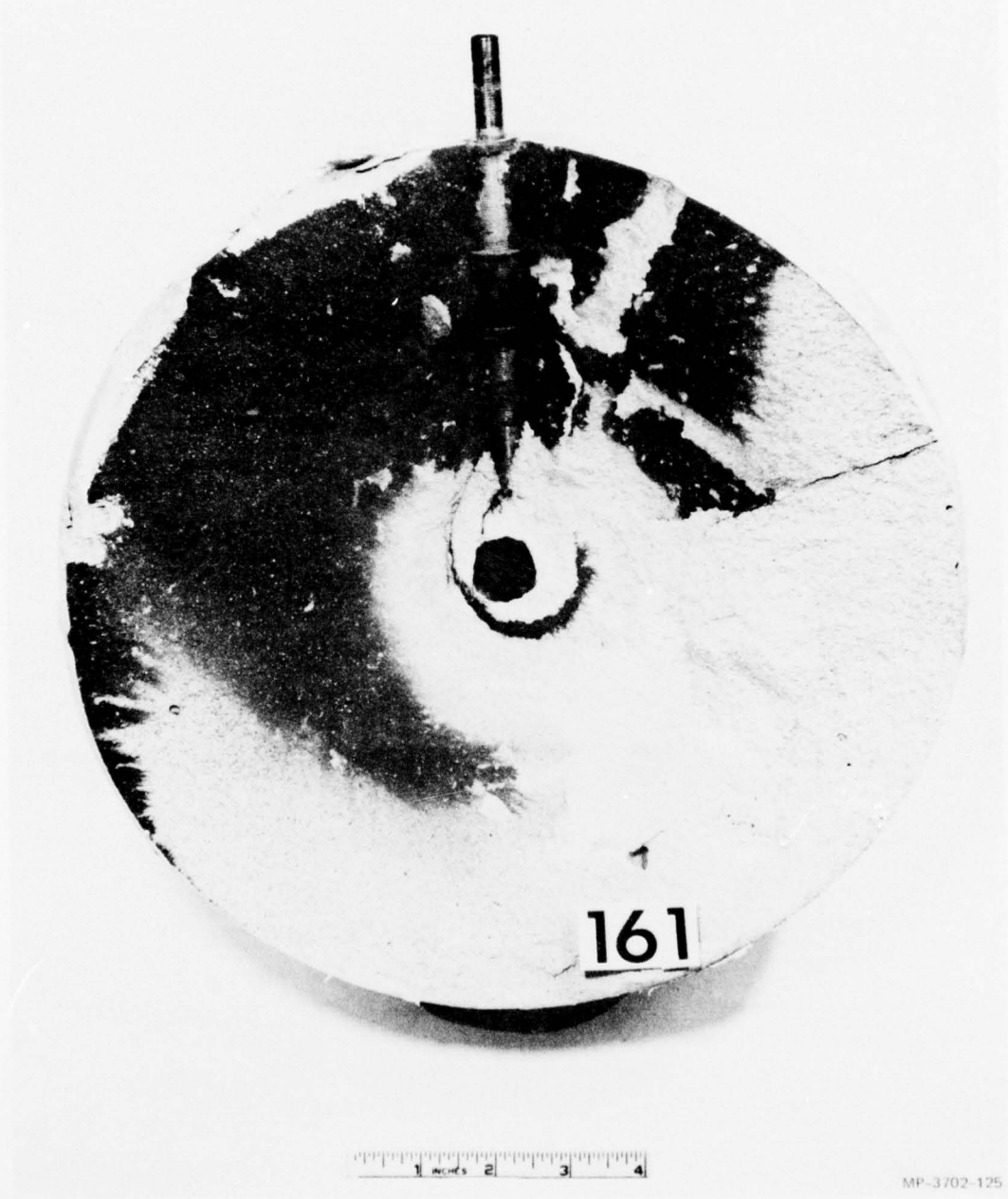

FIGURE 51 HYDROFRACTURE FROM LOCALITY AWAY FROM AN EXPLODED CAVITY TEST 161

MP-3702-126

FIGURE 51 HYDROFRACTURE FROM LOCALITY AWAY FROM AN EXPLODED CAVITY – TEST 161 (Concluded)

FIGURE 52 HYDROFRACTURE FROM LOCALITY AWAY FROM AN EXPLODED CAVITY – TEST 163

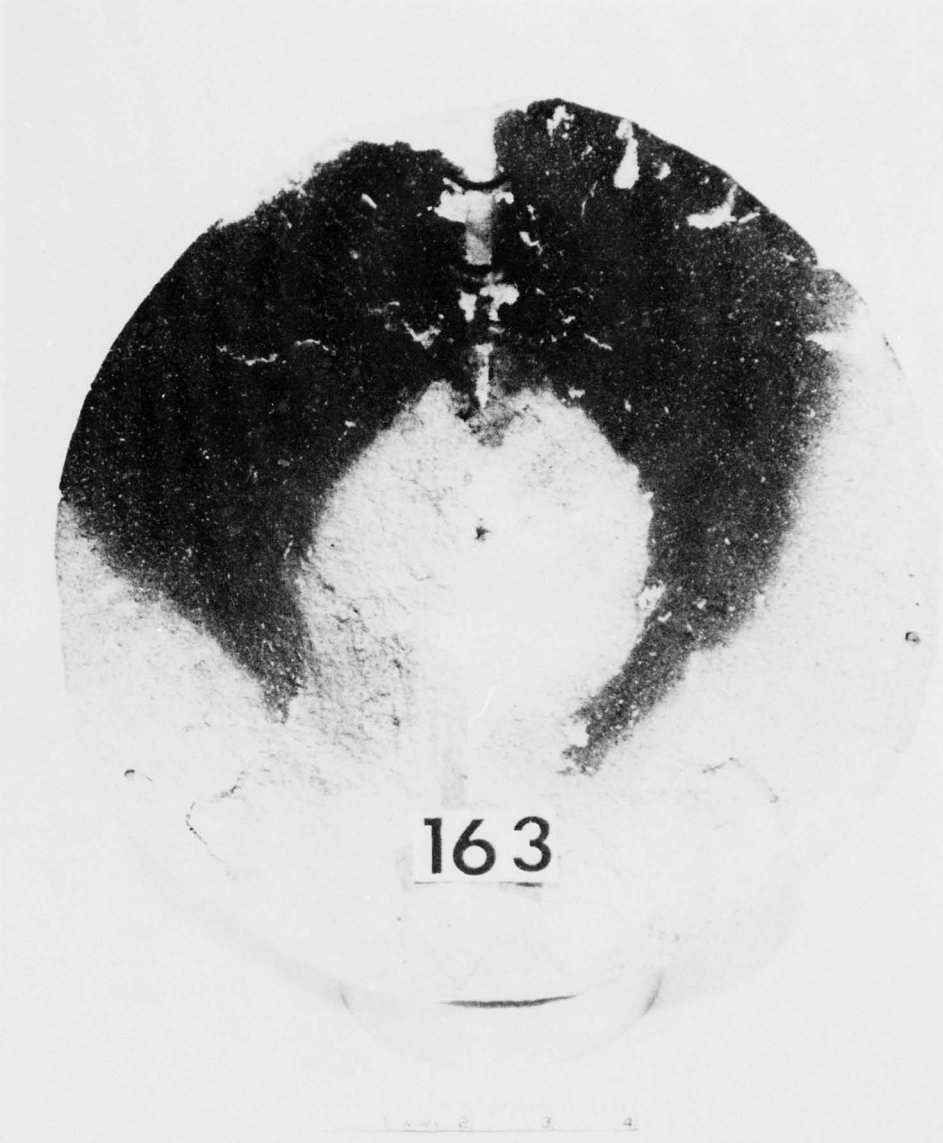

MP-3702-128

FIGURE 52 HYDROFRACTURE FROM LOCALITY AWAY FROM AN EXPLODED CAVITY – TEST 163 (Concluded)

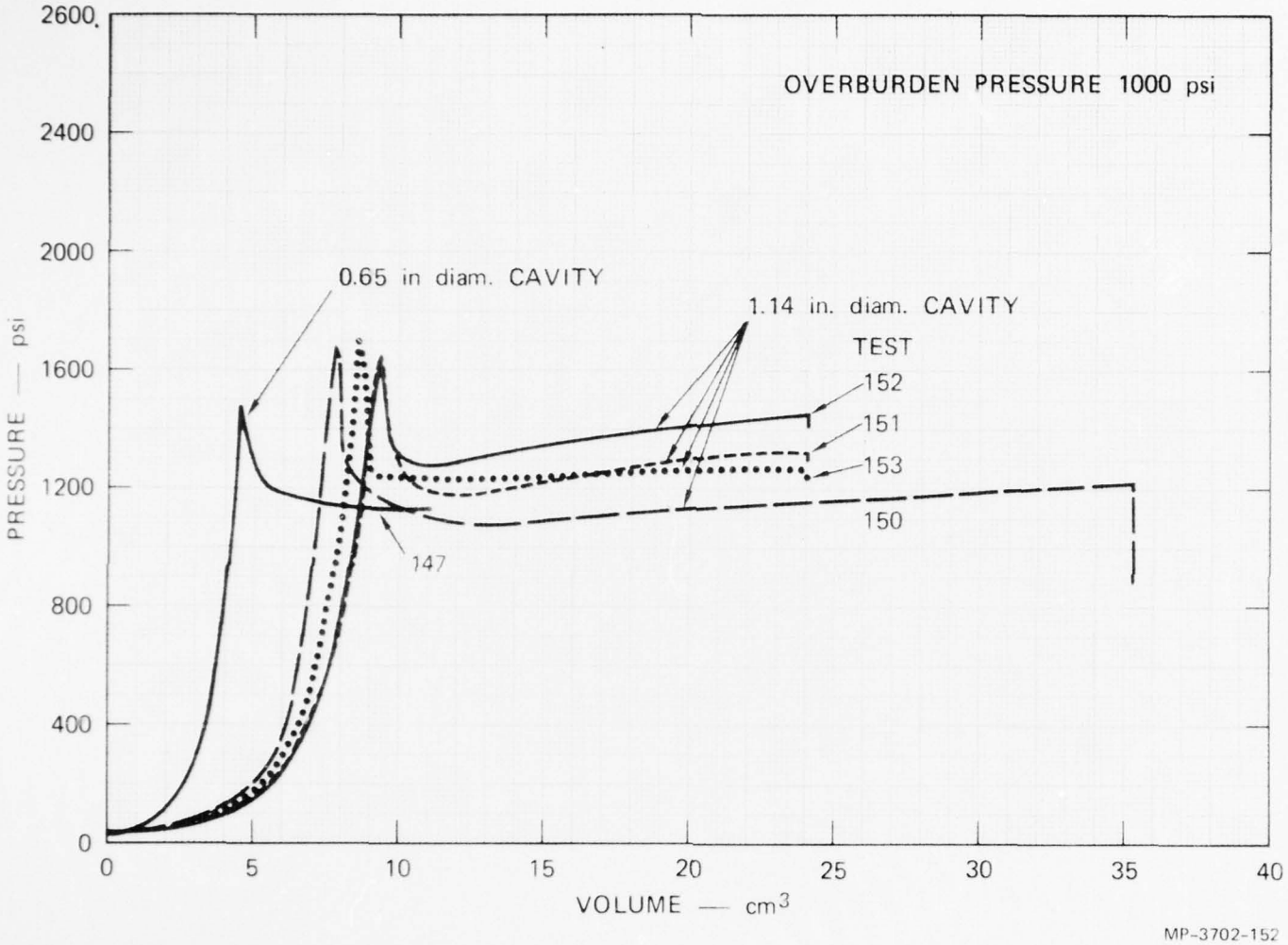

FIGURE 53 HYDROFRACTURE PRESSURES FOR UNEXPLODED CAVITY TEST 147 AND TESTS 150-153 – CAVITY VOLUME EFFECT

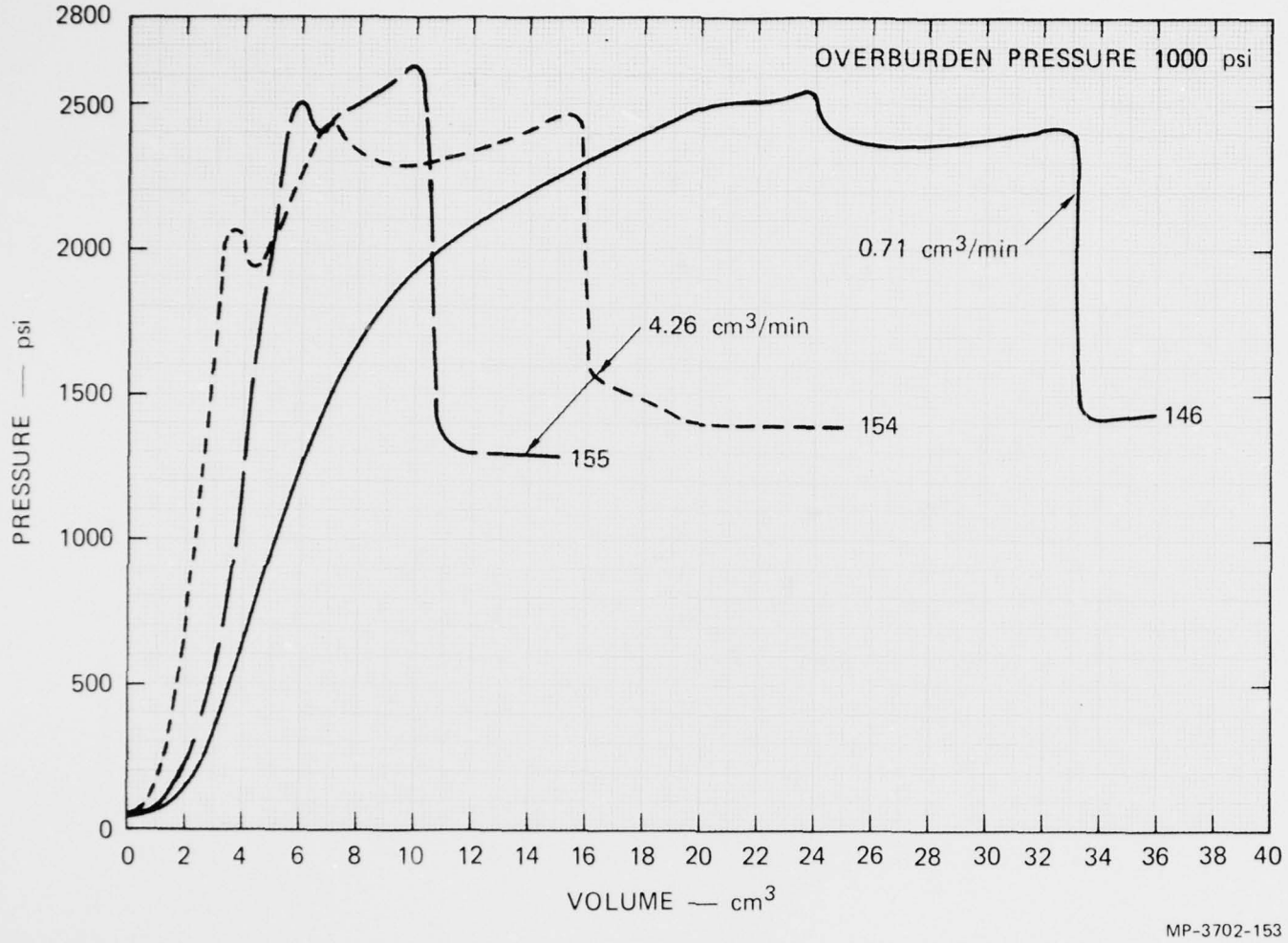

FIGURE 54 HYDROFRACTURE PRESSURES FOR EXPLODED CAVITY TESTS 146, 154, AND 155 – FLOW RATE EFFECT

V CONTAINMENT ANALYSIS

SRI Topical Report 3702-2 presents an analytical treatment of the dynamic expansion of a spherical cavity caused by an explosive pressure pulse. The analysis was performed to describe formation of the residual stress field and to establish dependence of the field on the parameters involved.

The analysis is a simple extension of the work of Hopkins[10] to describe rebound and a second expansion phase. Numerical data were chosen to correspond to the laboratory containment experiments described in Sections II-B and IV. Predictions for the final cavity radius are compared with experimental results. Predictions for cavity expansion history and stress distributions are compared with the predictions of a finite-difference code. Formulas are provided for the final cavity radius in terms of the explosive energy supplied and for the maximum tensile tangential stress and maximum compressive radial stress together with their locations at the end of the first expansion phase.

From the numerical examples and manipulation of the governing equations the following observations are made.

- Cavity expansion and contraction compared favorably with finite-difference code predictions (code included compressibility).
- Stress distributions when the cavity was fully expanded and fully contracted showed qualitative agreement with the code predictions. Quantitative differences arise because of the smaller ranges reached by the elastic-plastic interface in the code description, because volumetric plastic work is allowed.
- The final to initial radius ratio compares reasonably well with the experimental ratio.

- The simplest formula for the upper bound of the final to initial radius ratio, a_2/a_0, is

$$a_2/a_0 = (\bar{w}/4.3\,Y)^{1/3}$$

where $\bar{w}$ is the average initial energy density in the cavity and Y is the yield stress of the surrounding material. The radial ratio is thus independent of the material density, shear modulus, and overburden pressure.

- The simplest formulas for the maximum tangential stress σ_t and the maximum compressive radial stress σ_r, together with their locations R_2 and r_m at the end of the first expansion phase, are

$$0.9 - P_\infty/Y < \sigma_t/Y < 1.0 - P_\infty/Y$$

$$R_2/a_2 = (2G/Y)^{1/3}$$

$$\sigma_r/Y = -0.8 - P_2/Y$$

$$2.0 < r_m/a_2 < 2.3$$

where P_2 is the cavity pressure when fully expanded.

- Maxσ_t and max$(-\sigma_r)$ are independent of density and shear modulus and are approximately linearly dependent on the yield stress.

- Maxσ_t is reduced linearly by overburden pressure increase.

- Max$(-\sigma_r)$ depends linearly on the residual cavity gas pressure.

- R_2/a_2 is independent of density, cavity pressure, and overburden pressure.

- r_m/a_2 is restricted to a narrow range that is insensitive to all parameters.

A logical next step in the use of the analysis is to derive maximum stress and location formulas for the condition of full cavity contraction.

The next step to improve the analysis is to incorporate a tensile yield strength that is less than the compressive yield strength.

VI REFERENCES

1. R. W. Gates and C. F. Petersen, "A Laboratory Method for Studying Stemming of Line-of-Sight Tunnels in Underground Nuclear Tests," SRI Final Report DNA 3058Z, Contract DNA 001-72-C-0047 (November 1972).

2. R. W. Gates, C. F. Petersen, and A. L. Florence, "Laboratory Method for Studying Stemming of Line-of-Sight Tunnels in Underground Nuclear Tests," SRI Final Report DNA 3592F, Contract DNA 001-73-C-0122 (December 1973).

3. A. L. Florence, "Laboratory Investigation of Stemming of Horizontal Line-of-Sight (HLOS) Underground Nuclear Tests," SRI Final Report DNA 3684F, Contract DNA 001-74-C-0101 (February 1975).

4. A. L. Florence, "Laboratory Investigation of Stemming of Underground Nuclear Test," SRI Interim Report (DRAFT), Contract DNA 001-75-C-0083 (March 1976).

5. A. L. Florence and R. W. Gates, "Dynamic Grout Extrusion Experiments," SRI Topical Report TR-3702-4 (in preparation), Contract DNA 001-75-C-0083.

6. A. L. Florence and R. W. Gates, "Explosive Cavity Residual Stress Experiments," SRI Topical Report TR-3702-3 (in preparation), Contract DNA 001-75-C-0083.

7. A. L. Florence and T. C. Kennedy, "A Simple Analysis for Containment Studies," SRI Topical Report TR 3702-2 (DRAFT), Contract DNA 001-75-C-0083 (August 1976).

8. A. L. Florence, "On the Use of Photomechanics for Containment Studies," SRI Topical Report TR-3702-1 (DRAFT), Contract DNA 001-75-C-0083 (March 1976).

9. D. C. Erlich, "Three-Dimensional Seismic Modeling," SRI Final Report AFCRL-TR-0478, Contract F19628-74-C-0157 (August 1975).

10. H. G. Hopkins, "Dynamic Expansion of Spherical Cavities in Metals," in progress in Solid Mechanics, Vol. I, Chapter III, pp. 85-164, I. N. Sneddon and R. Hill, Eds. (Interscience Publishers, Inc., New York, 1960).

DISTRIBUTION LIST

DEPARTMENT OF DEFENSE

Director
Defense Nuclear Agency
ATTN: DDST
ATTN: STSI
3cy ATTN: STTL

Defense Documentation Center
12cy ATTN: TC

Commander
Field Command
Defense Nuclear Agency
ATTN: FCPR
ATTN: FCTMC, Carl Keller

Chief
Livermore Division, FCDNA
Lawrence Livermore Laboratory
ATTN: FCPRL

Chief
Test Construction Division
Field Command Test Directorate
Defense Nuclear Agency
ATTN: Joe LaComb

DEPARTMENT OF THE ARMY

Commander
Harry Diamond Laboratories
ATTN: DRXDO-NP

DEPARTMENT OF THE NAVY

Commander
Naval Surface Weapons Center
ATTN: Naval Nuclear Program Office

DEPARTMENT OF THE AIR FORCE

AF Weapons Laboratory, AFSC
ATTN: SUL

ENERGY RESEARCH & DEVELOPMENT ADMINISTRATION

University of California
Lawrence Livermore Laboratory
ATTN: David Oakley
ATTN: Billy Hudson
ATTN: Mr. Terhune

Los Alamos Scientific Laboratory
ATTN: Robert Brownlee
ATTN: Fred App

Sandia Laboratories
ATTN: Wendell Weart
ATTN: Lynn Tyler

U.S. Energy Research and Development Administration
Nevada Operations Office
ATTN: Robert Newman

DEPARTMENT OF DEFENSE CONTRACTORS

General Electric Company
TEMPO-Center for Advanced Studies
ATTN: DASIAC

Stanford Research Institute
ATTN: Alex Florence

Pacifica Technology
ATTN: G. I. Kent

Physics International Company
ATTN: E. T. Moore

Systems, Science & Software, Incorporated
ATTN: Russell E. Duff

Terra Tek, Incorporated
ATTN: Sidney Green